

Observations and comparisons with theory of the heliumlike and hydrogenlike resonance lines and satellites of nickel from the JET tokamak

F. Bombarda,* R. Giannella,* E. Källne, and G. J. Tallents†
JET Joint Undertaking, Abingdon, Oxfordshire OX14 3EA, England

F. Bely-Dubau and P. Faucher
Observatoire de Nice, Boîte Postale 139, F-06003 Nice Cédex, France

M. Cornille and J. Dubau
Observatoire de Paris-Meudon, F-92195 Meudon Principal Cédex, France

A. H. Gabriel
*Laboratoire de Physique Stellaire et Planétaire du Centre National de la Recherche Scientifique,
 F-91370 Verrières-le-buisson, France*

(Received 30 July 1987)

The resonance lines and heliumlike to boronlike satellites of heliumlike nickel and the Lyman- α doublet and heliumlike satellites of hydrogenlike nickel emitted from the JET tokamak have been recorded with good spectral resolution ($\lambda/\Delta\lambda=20\,000$). Atomic data (wavelengths and intensity factors) for the dielectronic and other satellites are calculated in a multiconfiguration intermediate-coupling scheme with use of scaled Thomas-Fermi-Dirac potentials and compared with the experimental spectra. Overall good agreement between theory and the experimental spectra is obtained, though the intensities of satellites to the heliumlike lines indicate that the populations of the lithiumlike to boronlike ions relative to the heliumlike populations are greater than expected for a coronal ionization balance. Possible causes of this discrepancy are departures from coronal equilibrium due to charge exchange with neutral hydrogen atoms or departures from coronal equilibrium due to transport of lower ionization stages of nickel impurities from the tokamak edge to the center at a rate greater than predicted by other diagnostics.

I. INTRODUCTION

The electron temperatures produced in tokamaks now are sufficient to ionize many metallic impurity elements to the hydrogenlike or heliumlike state. Spectroscopy of the x-ray emission from these ions has become a useful technique for determining ion temperatures, bulk plasma movement and the dynamics of plasma-impurity transport in the central (peak temperature) regions of the plasmas. X-ray spectra from tokamaks are also of importance in comparison with equivalent spectra from astrophysical plasmas as the tokamak plasma densities and temperatures are usually well characterized by many diagnostics and can, to a certain extent, be controlled.

With use of high-resolution crystal spectrometers, heliumlike and hydrogenlike spectra of heavy impurities have been obtained from several large tokamaks (see Källne and Källne¹ for a recent comprehensive review). At the Joint European Torus (JET) the high electron temperatures achieved have enabled the observation of heliumlike and hydrogenlike nickel ($Z=28$), currently the highest atomic number hydrogenlike and heliumlike spectra observed from tokamaks. In this paper these spectra are presented and discussed. Heliumlike nickel spectra have been obtained with poor spectral resolution

in a vacuum spark² and with good resolution also in the TFTR tokamak.³ However, hydrogenlike nickel spectra have so far only been recorded at JET.

Calculated atomic data (wavelengths and intensity factors) for the dielectronic and other satellites close to the heliumlike and hydrogenlike nickel resonance lines are also presented here. These data are used to generate theoretical spectra which are compared with experimental observations from the JET tokamak of the heliumlike and hydrogenlike nickel spectra.

II. EXPERIMENT

A. Plasma

The JET is a large tokamak designed to achieve thermonuclear plasma heating.⁴ Plasma discharges with record toroidal currents up to 5 MA and magnetic fields up to 3.5 T have been produced so far and a wide range of plasma parameters have been explored in different operating schemes. Hydrogen and deuterium discharges with carbon or magnetic limiters are additionally heated by electromagnetic waves in the ion cyclotron frequency range and by injection of neutral hydrogen and deuterium beams.^{5,6} The record value of the fusion parameter $n_D\tau_E T_i = 2 \times 10^{20} \text{ m}^{-3} \text{ sec keV}$ (with n_D peak deuterium

density, τ_E energy confinement time, T_i peak ion temperature) has recently been achieved in neutral-beam-heated discharges.⁷

The experimental data acquired in 1986 from JET are representative of most of the plasma conditions obtained so far: peak electron densities N_e in the range $(1.5-6.0) \times 10^{19} \text{ m}^{-3}$ and peak electron and ion temperatures in the ranges $T_e = 1.8-7 \text{ keV}$ and $T_i = 1.5-15 \text{ keV}$, respectively. Horizontal minor radii of the toroidal plasmas have been obtained in the range from 0.90–1.20 m with an elongation of the *D* shaped cross section in the range 1.0–1.9 and with major radii of the magnetic axis varying from 2.8 to 3.5 m. The duration of the discharges is usually longer than 15 sec with steady-state conditions lasting up to slightly shorter time intervals.⁴

In order to reduce to a minimum the release of metallic impurities into the discharge, the JET inconel (Ni ~ 72%, Cr ~ 15%, Fe ~ 8%) vacuum vessel is protected from contact with the plasma by eight carbon limiters on the large major radius side (the outer side) and by a wall of graphite tiles on the inner side. A treatment of carbonization⁸ of all the surfaces in the discharge chamber has also been repeatedly applied. Consequently, the impurity content in the plasma is dominated by light elements (oxygen and carbon), reducing the nickel, chromium, and iron content relative to the electron density to trace concentration values of $\sim 10^{-5}$ to $\sim 5 \times 10^{-4}$ as deduced from line-intensity measurements of the X-ray crystal spectrometer and other spectroscopic instruments.⁹ Nevertheless, due to the high electron temperatures, the large size of the emitting plasma and the high throughput of the crystal spectrometer, the resonance line of He-like Ni is readily observed and the Ni ion temperature and the toroidal rotation velocity are routinely determined through the measurement of line broadening and line shift of the He-like resonance line.¹⁰ Experiments to obtain ion temperatures from the profiles of the H-like Lyman- α doublet have also been undertaken when high electron temperatures produced sufficient intensities.

B. Crystal spectrometer

In Fig. 1 the line of sight of the spectrometer through the JET plasma is shown. The line of sight lies in the tokamak equatorial plane and reaches the minimum distance of approach to the torus axis of symmetry $R_0 = 1.82 \text{ m}$ within the vacuum vessel at the plasma inner edge. The plasma column is seen twice with the toroidal direction making opposite angles with the line of sight. The cross section of the plasma seen by the spectrometer is roughly 20 cm in width and 10 cm in height.

The orientation of the observation line, the Bragg angle used (in the range from 48.75° to 52.75°) and the spectrometer size were imposed by the requirement to keep both the crystal dispersing element and the detector outside the hostile environment of the JET torus hall. This measure enables accessibility of personnel to the instrument and is expected to be necessary in order to keep the radiation-induced noise on the detector

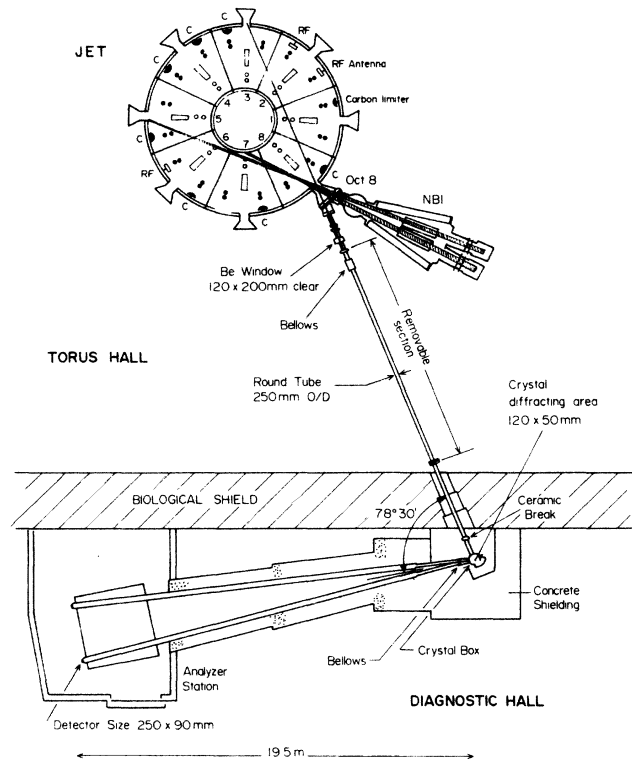


FIG. 1. Plan of the x-ray crystal spectrometer and the JET tokamak. Important components are labeled and the line of sight through the plasma is shown.

within tolerable levels in the planned deuterium-tritium phase of JET operation.

A detailed description of the spectrometer will be given in a separate paper.¹¹ Here we only give details of relevance for the present experimental data.

The instrument is a bent crystal spectrometer of the Johann type.¹² The crystal, positioned just outside a penetration through the JET torus hall 3-m-thick shielding wall, looks at the plasma source through a beryllium window 150 μm thick located at one of the tokamak main horizontal ports. The ray path runs within a 30-cm-diameter evacuated tube from the beryllium window to the crystal vacuum box. The x rays are diffracted from the crystal mounted on a turntable and reach the detector through another evacuated tube pivoted about an axis next to the crystal vacuum box to match the diffracted x-ray direction according to the Bragg angle fixed by the crystal orientation. The distance between the focal position, located at the throat of the torus port at the beryllium window, and the crystal itself is about 20 m; an equal distance from the detector is imposed by the Johann focusing geometry. This distance, together with the Bragg angle, leads to a fractional linear dispersion $(1/\lambda)(\Delta\lambda/\Delta x)$ of about $4 \times 10^{-4} \text{ cm}^{-1}$.

In the Johann configuration of the spectrometer, different x-ray wavelengths pass through different positions on the beryllium window and the window extension in the focal plane of 20 cm defines the instrument spectral range. The spectral range when the instrument is

set to view the He-like Ni resonance line is 12 mÅ (a bandwidth $\Delta\lambda/\lambda$ of 0.8%).

A quartz crystal cut parallel to the $2\bar{2}4\bar{3}$ plane ($2d=2.0296$ Å) was used in the experiments discussed here. It is curved to a radius of curvature of 25.25 m with the bending device described in Ref. 13 and has an effective diffracting area of 5 cm by 12 cm. The detector is a multiwire proportional chamber where each anode wire is connected to an independent amplification and counting chain, thus providing a high-counting-rate (up to 250 kHz per wire) position-sensitive photon detection. The anode spacing of 0.127 cm is the dominant resolution-limiting factor leading to an instrumental resolution $\lambda/\Delta\lambda \approx 20\,000$.

C. Measurements

Due to the small angular acceptance of the spectrometer which is limited by the beryllium window size allowed to the tokamak, the full spectrum of He-like nickel between 1.584 and 1.621 Å was taken by setting the instrument to observe at five different, adjacent wavelengths (with overlapping wavelength ranges) during a sequence of very similar, consecutive JET discharges [Fig. 2(a)]. For each wavelength setting, at least one spectral line also appears on the adjacent spectra, thus allowing the wavelength and intensity repeatability of the measurements to be assessed and some small intensity normalization (changes < 10%) between pulses to be undertaken. [Some small intensity differences can be observed in the spectrum at the joining points, Fig. 2(a).] The main plasma parameters were the toroidal field $B_T=2.8$ T, plasma current $I_p=3.0$ MA, central line integrated density $\int N_e dl=6.0 \times 10^{19}$ m⁻², and peak electron temperature measured from electron cyclotron emission $T_e=3.1$ keV. A Ni ion temperature of 2.4 keV was measured from the Doppler broadening of the resonance line w fitted with a Voigt profile.

The H-like nickel spectrum between 1.525 and 1.545 Å [Fig. 2(b)] was obtained in two consecutive pulses with $B_T=3.4$ T, $I_p=4$ MA, $\int N_e dl=6.0 \times 10^{19}$ m⁻², and $T_e=4.7$ keV. A Ni ion temperature of 4.0 keV was measured from the Doppler broadening of the Lyman- α_1 component.

The conversion from channel position in the detector to wavelength λ can be obtained using Bragg's law and simple geometry. We have

$$\lambda = 2d \sin(\theta_0 + x_n/L), \quad (1)$$

where d is the crystal reflecting atomic plane spacing, θ_0 is the measured angle between the crystal surface and the central line of sight, L is the measured distance between crystal and detector, and x_n is the distance of the n th channel from the center of the detector. Errors in the measurement of absolute wavelengths are caused by the following.

(i) Mechanical irregularities of the crystal rotation mechanism and errors in the detector and crystal posi-

tion encoding causing errors in the measured values of θ_0 and L giving rise to wavelength setting errors in the spectrometer of $\sim \pm 0.4$ mÅ.

(ii) Uncertainty in the crystal $2d$ value. A literature survey of $2d$ values for the quartz diffraction plane used ($2\bar{2}4\bar{3}$) indicates that $2d=2.0296 (\pm 0.0004)$ Å at 18°C with a possible further variation of the $2d$ value of ± 0.00014 Å due to temperature effects in the range from 13°C to 23°C. This gives a total maximum uncertainty of ± 0.5 mÅ in the crystal $2d$ value which implies a wavelength measurement error of ± 0.4 mÅ for wavelengths in the range 1.5–1.7 Å.

(iii) Uncertainty in θ_0 .

(a) Initial alignment. The “zero” angular position of the crystal has been determined by autocollimation of a reference laser beam reflected from the crystal surface. This procedure is estimated to allow absolute θ_0 to be determined to within 0.03°. Such an angular error introduces a systematic error in absolute wavelengths of $\sim \pm 0.7$ mÅ. In addition, there is an error here due to the initial position encoding of $\sim \pm 0.4$ mÅ.

(b) Degree of parallelism of the crystal surface with respect to the atomic planes. Deviations of $0 \pm 0.0085^\circ$ of the crystal surface to the crystal planes have been measured at several points across the crystal surface with an x-ray goniometer for the particular crystal employed in these measurements. Such deviations will introduce a wavelength error of up to $\sim \pm 0.2$ mÅ.

(iv) Other possible errors. Errors due to the variation of lattice parameters caused by the curvature of the crystal and the effects of refraction in the crystal are negligible compared to the above effects.

By quadratically adding up to the above error contributions, the total error in the absolute value of the helium and hydrogenlike resonance line wavelengths can be estimated at ± 1.0 mÅ. However, the relative precision on the distance in wavelength of satellite lines from the resonance line is estimated to be ± 0.08 mÅ—more than an order of magnitude smaller. This relative wavelength error depends almost entirely on the accuracy in the determination of the peak position of the spectral lines (and, where applicable, errors in overlapping different sections of the spectrum) as errors in the dispersion are negligible.

III. COMPUTATION OF ATOMIC DATA

In the wavelength range of the experimental heliumlike spectrum [Fig. 2(a)], characteristic lines of nickel arising from the heliumlike stage as well as inner-shell and dielectronic satellite lines from the lithiumlike, berylliumlike, and boronlike ionization stages are contained. These lines are all produced by an electronic transition $n=2$ to 1 in the presence of an additional 1s electron for the He-like stage plus 1, 2, or 3 electrons in shells $n \geq 2$ for the other stages. Thus, this region contains a large number of lines from many ionization stages. To compute the spectra, it is necessary to calculate the wavelengths of all the lines and evaluate their intensities by computing the rates for all processes leading

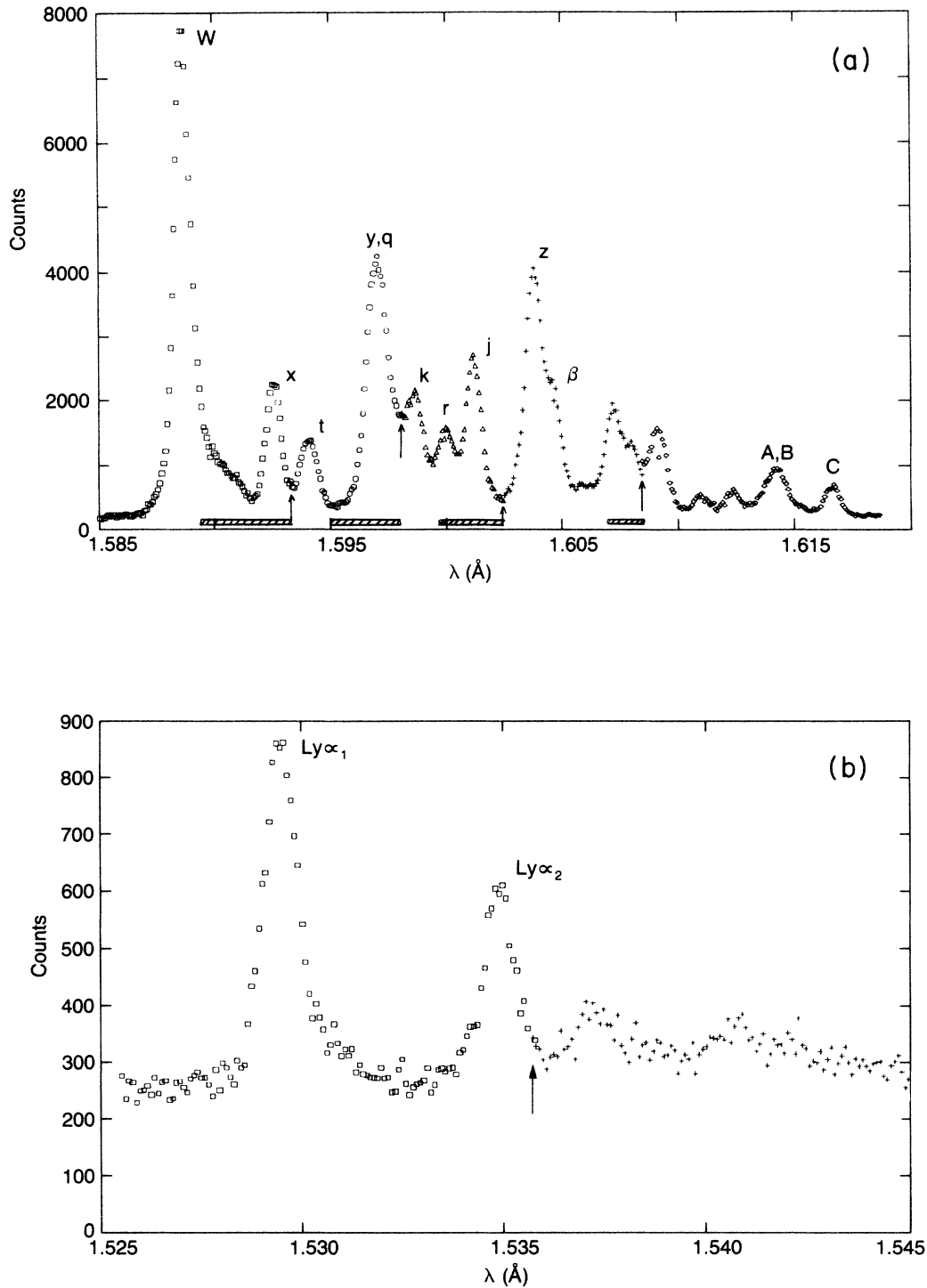


FIG. 2. Spectra emitted from JET and recorded by the x-ray crystal spectrometer during steady-state ohmic discharges. The spectral ranges recorded during different discharges are separated by arrows. (a) The spectrum near the resonance line of helium-like nickel. The spectral lines are labeled with the notation of Gabriel (Ref. 20) and with notation introduced in the text. The spectrum is obtained by integrating the emission over nine seconds from a plasma with peak electron temperature ~ 3 keV and peak electron density $\sim 2 \times 10^{13} \text{ cm}^{-3}$ (see text). The arrows indicate joining points for the five different spectra for this composite figure. The spectra were joined with overlapping regions as shown as hatched regions. The data are shown without any normalization between the spectra being undertaken. (b) The spectrum near the resonance lines of hydrogenlike nickel. The Lyman- α_1 and - α_2 components are labeled. The spectrum is obtained by integrating the emission over ten seconds from a plasma with peak electron temperature of approximately 4.7 keV and peak electron density of approximately $1.5 \times 10^{13} \text{ cm}^{-3}$. The arrows indicate the joining point of the two spectra used to build the full spectrum.

to their emission. In Sec. III A we describe the derivation of the important atomic parameters of wavelengths, transition probabilities for radiative and autoionization decay, and collisional excitation rates, together with the relations important for understanding the intensities of the spectral lines. A more complete treatment of the theory can be found in earlier papers for calcium¹⁴ and chromium.¹⁵

In the wavelength range of the experimental hydrogenlike spectrum [Fig. 2(b)], the Lyman- α doublet arising from the hydrogenlike stage and heliumlike dielectronic satellites are contained. The lines are again all produced by an electron transition $n=2$ to 1 plus one electron in shells $n \geq 2$ for the heliumlike satellites. In Sec. III B the computed wavelengths and results necessary to calculate the intensities for the hydrogenlike spectra are presented.

The problem of deriving the distribution of ionization stages and of integrating along the spectrograph line of sight in order to simulate the experimental spectrum is considered in Sec. IV.

A. Heliumlike spectrum

1. Calculation of the atomic parameters

Wavelengths λ and radiative transition probabilities A , have been calculated using the program SUPERSTRUCTURE developed by Eissner *et al.*¹⁶ The program includes in the Hamiltonian some of the Breit Pauli relativistic corrections. The autoionization probabilities A_a for all available continua have been obtained using the program AUTOLSI described in the paper by the TFR group *et al.*¹⁵ These two programs use the same wave functions and model potentials and are well suited for the computation of large quantities of atomic data for multiply charged ions. They use scaled Thomas-Fermi Dirac potentials for which the scaling parameters λ_l are determined by an energy minimization of all the terms of the following configurations:

$$1s^2 2s, 1s 2s 2p, 1s^2 3d, 1s 2p 3d,$$

giving scaling factors of $\lambda_s = 2.737$, $\lambda_p = 2.176$, and $\lambda_d = 1.940$ ($\lambda_g = \lambda_f = \lambda_d$). The mono-electron wave functions obtained in this way have also been used for the two-, three-, four-, and five-electron ions. The present atomic data have been calculated using multiconfiguration expansions containing, for the three-electron system, the configurations $(1s^2 nl)$ and $(1s 2l') nl''$ with $n \leq 5$; for the four-electron system, the configurations $(1s^2 2l) nl'$ and $(1s 2l 2l') nl''$ with $n \leq 4$; and for the five-electron system, only the six configurations $1s^2 2s^2 2p$, $1s^2 2s 2p^2$, $1s^2 2p^3$, $1s 2s^2 2p^2$, $1s 2s 2p^3$, and $1s 2p^4$. Excitation rates by electronic collision have been calculated using DISTORTED WAVE¹⁷ and JJOM,¹⁸ the details of which are described elsewhere.¹⁹

2. Heliumlike lines

Transitions from the excited states $1s 2p^1 P_1$, $1s 2p^3 P_{2,1}$, and $1s 2s^3 S_1$, to the ground state $1s^2^1 S_0$ give

rise to four spectral lines, respectively w , x , y , and z , using the notation of Gabriel.²⁰

These lines are excited by electron impact from the ground state $1s^2^1 S_0$ (no metastable ground states are considered here), involving three distinct processes: (i) direct excitation, (ii) so-called "resonance effects," involving the temporary formation of three-electron states which decay rapidly by autoionization to give the excited level, and (iii) cascade effects, involving the temporary excitation to higher excited states $1snl$, followed by successive radiative decay to produce the required $1s 2l'$ state. The process (ii) has been evaluated for resonances of the type $1s 3l' nl$ ($1sn'l' nl$ with $n' \geq 4$ resonances are negligible) using the method described by Faucher and Dubau.²¹ Process (ii) contributes to the lines x , y , and z , but mostly to z . Cascade effects contribute to all lines, but again mostly to the x , y , and z lines. All such processes can be represented by a partial or total effective excitation rate coefficient C in $\text{cm}^3 \text{s}^{-1}$, such that the emissivity (intensity emitted in photons per unit volume) is given by

$$\epsilon = N_e N_z C, \quad (2)$$

where N_e and N_z are densities of electrons and the target ion, in this case Ni XXVII. Table I lists values of C for each line as a function of electron temperature T_e identifying the contributions of each of the three exciting processes.

A further small contribution to the intensity of the heliumlike lines arises through recombination, both radiative and dielectronic, from hydrogenlike Ni XXVIII. This contribution has been examined using the theory described for iron.²² Table II lists the effective rate coefficients α for recombination involved in the emission of the four heliumlike lines. Another process exists for exciting the line z only, namely, inner-shell ionization of the lithiumlike ion Ni XXVI. This rate coefficient S (also shown in Table II) was determined using the Lotz formula. Including these two other population processes Eq. (2) becomes

$$\epsilon = N_e (N_z C + N_{z+1} \alpha + N_{z-1} S). \quad (2')$$

3. Dielectronic satellite lines

Configurations having a vacancy in the $1s$ shell can decay either by radiation (emitting a satellite line) or by autoionization. Such configurations in general have two alternative excitation mechanisms: inner-shell excitation from the ground state of the ion, and dielectronic recombination from the ion stage above. While both processes can be important, many satellite lines have one or the other dominant. Now we discuss excitation by dielectronic recombination, which is the dominant process for the majority of the satellites.

The emissivity ϵ_d of a dielectronic satellite line emitted by Ni XXVI ionized atom is obtained by using the formula

$$\epsilon_d = N_e N_z F_1^*(T_e) F_2^*(s), \quad (3)$$

where

TABLE I. Ni XXVII effective excitation rate coefficients, C ($\text{cm}^3 \text{sec}^{-1}$) for the lines w , x , y , and z . (a) Direct excitation. (b) Direct excitation and resonances. (c) Direct excitation, resonances, and cascades. The notation w, x, y, z is from Ref. 20 and the wavelengths are as calculated. Numbers in square brackets are powers of ten, e.g., $0.210[-17]=0.210 \times 10^{-17}$.

T_e (keV)	z (1.6010 Å)			y (1.5941 Å)		
	(a)	(b)	(c)	(a)	(b)	(c)
0.6	0.210[-17]	0.332[-17]	0.623[-17]	0.498[-17]	0.560[-17]	0.566[-17]
1.0	0.272[-15]	0.397[-15]	0.867[-15]	0.678[-15]	0.748[-15]	0.771[-15]
1.4	0.202[-14]	0.279[-14]	0.684[-14]	0.523[-14]	0.568[-14]	0.598[-14]
1.8	0.591[-14]	0.785[-14]	0.210[-13]	0.158[-13]	0.170[-13]	0.182[-13]
2.2	0.114[-13]	0.147[-13]	0.433[-13]	0.311[-13]	0.331[-13]	0.355[-13]
2.6	0.179[-13]	0.225[-13]	0.661[-13]	0.492[-13]	0.520[-13]	0.562[-13]
3.0	0.249[-13]	0.303[-13]	0.920[-13]	0.683[-13]	0.718[-13]	0.776[-13]
3.4	0.320[-13]	0.382[-13]	0.116[-12]	0.871[-13]	0.911[-13]	0.988[-13]
3.8	0.392[-13]	0.460[-13]	0.140[-12]	0.105[-12]	0.109[-12]	0.120[-12]
4.2	0.464[-13]	0.538[-13]	0.163[-12]	0.122[-12]	0.127[-12]	0.139[-12]
4.6	0.533[-13]	0.610[-13]	0.182[-12]	0.137[-12]	0.142[-12]	0.156[-12]
5.0	0.601[-13]	0.681[-13]	0.197[-12]	0.151[-12]	0.156[-12]	0.174[-12]
6.0	0.757[-13]	0.835[-13]	0.239[-12]	0.181[-12]	0.186[-12]	0.210[-12]

T_e (keV)	x (1.5897 Å)			w (1.5856 Å)		
	(a)	(b)	(c)	(a)	(b)	(c)
0.6	0.617[-17]	0.719[-17]	0.618[-17]	0.143[-16]	0.150[-16]	0.151[-16]
1.0	0.817[-15]	0.934[-15]	0.826[-15]	0.218[-14]	0.226[-14]	0.231[-14]
1.4	0.608[-14]	0.684[-14]	0.621[-14]	0.184[-13]	0.189[-13]	0.195[-13]
1.8	0.176[-13]	0.195[-13]	0.182[-13]	0.595[-13]	0.608[-13]	0.631[-13]
2.2	0.335[-13]	0.368[-13]	0.347[-13]	0.125[-12]	0.127[-12]	0.132[-12]
2.6	0.509[-13]	0.555[-13]	0.525[-13]	0.209[-12]	0.212[-12]	0.219[-12]
3.0	0.678[-13]	0.736[-13]	0.708[-13]	0.304[-12]	0.308[-12]	0.327[-12]
3.4	0.832[-13]	0.898[-13]	0.871[-13]	0.405[-12]	0.409[-12]	0.436[-12]
3.8	0.966[-13]	0.104[-12]	0.101[-12]	0.507[-12]	0.512[-12]	0.537[-12]
4.2	0.108[-12]	0.116[-12]	0.115[-12]	0.609[-12]	0.614[-12]	0.645[-12]
4.6	0.117[-12]	0.125[-12]	0.126[-12]	0.708[-12]	0.713[-12]	0.741[-12]
5.0	0.125[-12]	0.133[-12]	0.138[-12]	0.803[-12]	0.808[-12]	0.841[-12]
6.0	0.137[-12]	0.145[-12]	0.153[-12]	0.102[-11]	0.103[-11]	0.106[-11]

$$F_1^*(T_e) = \frac{1}{2} \left(\frac{2\pi\hbar^2}{mkT_e} \right)^{3/2} \exp \left(\frac{-E_s}{kT_e} \right),$$

$$F_2^*(s) = \frac{g_s}{g_i} \frac{A_a^{si} A_r^{sf}}{\sum_{i'} A_a^{si'} + \sum_{f'} A_r^{sf'}} \quad (\text{line factor}).$$

m , k , and h are the usual physical constants, g_s is the statistical weight of the upper level s of the line sf , g_i is that of the ground state of the ion Z , and E_s is the energy of the free electron produced by the autoionization process. The sum over i' extends over all levels of the (Z) ion accessible by autoionization from the state s .

TABLE II. Effective recombination rate coefficients α from H-like nickel into the upper quantum states for the w , x , y , and z lines and the ionization rate coefficient S_Z from Li-like $1s^2 2s$ nickel to the upper quantum state for the z line in units of $\text{cm}^3 \text{sec}^{-1}$. Numbers in square brackets are powers of ten, e.g., $1.26[-12]=1.26 \times 10^{-12}$.

T_e (keV)	α_w	α_x	α_y	α_z	S_z
0.6	1.26[-12]	1.79[-12]	1.27[-12]	2.10[-12]	3.541[-20]
1.0	8.05[-13]	1.14[-12]	8.08[-13]	1.43[-12]	4.218[-17]
1.4	6.07[-13]	8.52[-13]	5.99[-13]	1.12[-12]	9.164[-16]
1.8	5.03[-13]	6.89[-13]	4.83[-13]	9.46[-13]	5.175[-15]
2.2	4.40[-13]	5.87[-13]	4.09[-13]	8.32[-13]	1.576[-14]
2.6	3.96[-13]	5.16[-13]	3.58[-13]	7.51[-13]	3.434[-14]
3.0	3.62[-13]	4.62[-13]	3.20[-13]	6.89[-13]	6.108[-14]
3.4	3.35[-13]	4.20[-13]	2.90[-13]	6.38[-13]	9.522[-14]
3.8	3.12[-13]	3.85[-13]	2.65[-13]	5.95[-13]	1.355[-13]
4.2	2.91[-13]	3.55[-13]	2.44[-13]	5.57[-13]	1.807[-13]
4.6	2.73[-13]	3.30[-13]	2.26[-13]	5.24[-13]	2.295[-13]
5.0	2.57[-13]	3.07[-13]	2.10[-13]	4.94[-13]	2.809[-13]
6.0	2.23[-13]	2.62[-13]	1.79[-13]	4.33[-13]	4.150[-13]

The sum over f' relates to all lower states of the ion $Z-1$. It can readily be shown^{20,23} that at the electron densities found in low-density plasmas such as tokamaks, the local emissivity of a pure dielectronic satellite line relative to the parent resonance line w depends on T_e , independent on N_e or N_Z . For Ni XXV or Ni XXIV satellites, the emissivity is given by a formula similar to Eq. (3) but where the ionization degree Z is replaced by $Z-1$ or $Z-2$, respectively.

Table III(a) gives the Ni XXVI $n=2$ dielectronic satellite atomic data obtained by diagonalization of a large basis set including all of the $n=2,3,4,5$ configurations. Data from the same computation for $n=3,4$, and 5 are

given in Tables III(b), III(c), and III(d) where the values for λ , $F_2^*(s)$, and E_s only are listed.

Satellites for $n > 5$ form four series of lines which converge at the wavelengths of the parent transitions w and y . These are in general not resolvable, but contribute to the observed intensity of w and y . An extrapolation technique¹⁹ has been used to derive the total line factors (according to the parity of the configuration of the autoionizing level). These are given in Table IV. In the same way, satellites due to berylliumlike Ni XXV are computed and listed in Tables V(a), V(b), and V(c) using methods described in Ref. 24. Finally, the data for boronlike Ni XXIV $n=2$ satellites are given in Table VI.

TABLE III. (a) Ni XXVI $n=2$ dielectronic satellite data. A_o , A_r , and $F_2(s)$ are in units of 10^{13} sec^{-1} . Key letters are from Ref. 20. The energy E_s of the upper quantum state is relative to the ground state of the heliumlike ion. (b) Ni XXVI $n=3$ strong dielectronic satellites (only lines with line factors of 1/100 or larger than the strongest satellite are listed). (c) Ni XXVI $n=4$ strong dielectronic satellite lines. (d) Ni XXVI $n=5$ strong dielectronic satellite lines.

(a)							
Transitions	Key letter	A_o	A_r	$\sum A_r$	$F_2^*(s)$	λ (Å)	E_s (keV)
$1s2p^2 2P_{3/2} - 1s^2 2p^2 2P_{3/2}$	a	3.75	83.5	84.7	14.2	1.5950	5.4495
$1s2p^2 2P_{3/2} - 1s^2 2p^2 2P_{1/2}$	b	3.75	1.17	84.7	0.20	1.5899	5.4495
$1s2p^2 2P_{1/2} - 1s^2 2p^2 2P_{3/2}$	c	0.12	20.1	93.3	0.05	1.6004	5.4232
$1s2p^2 2P_{1/2} - 1s^2 2p^2 2P_{1/2}$	d	0.12	73.2	93.3	0.19	1.5953	5.4232
$1s2p^2 4P_{5/2} - 1s^2 2p^2 2P_{3/2}$	e	3.39	6.65	6.65	13.5	1.6046	5.4033
$1s2p^2 4P_{3/2} - 1s^2 2p^2 2P_{3/2}$	f	0.21	1.48	1.50	0.73	1.6066	5.3937
$1s2p^2 4P_{1/2} - 1s^2 2p^2 2P_{1/2}$	i	0.02	4.28	4.32	0.04	1.6040	5.3811
$1s2p^2 2D_{5/2} - 1s^2 2p^2 2P_{3/2}$	j	13.8	27.4	27.4	55.0	1.5983	5.4337
$1s2p^2 2D_{3/2} - 1s^2 2p^2 2P_{1/2}$	k	13.2	44.1	49.6	37.1	1.5956	5.4218
$1s2p^2 2D_{3/2} - 1s^2 2p^2 2P_{3/2}$	l	13.2	5.49	49.6	4.62	1.6007	5.4218
$1s2p^2 2S_{1/2} - 1s^2 2p^2 2P_{3/2}$	m	3.06	36.0	36.8	5.53	1.5910	5.4692
$1s2p^2 2S_{1/2} - 1s^2 2p^2 2P_{1/2}$	n	3.06	0.8	36.8	0.12	1.5859	5.4692
$1s2s^2 2S_{1/2} - 1s^2 2p^2 2P_{3/2}$	o	13.8	0.94	2.15	1.64	1.6252	5.3052
$1s2s^2 2S_{1/2} - 1s^2 2p^2 2P_{1/2}$	p	13.8	1.19	2.15	2.06	1.6199	5.3052
$1s2p2s(1P)^2 P_{3/2}^0 - 1s^2 2s^2 2S_{1/2}$	q	0.10	64.8	64.8	0.42	1.5941	5.3770
$1s2p2s(1P)^2 P_{1/2}^0 - 1s^2 2s^2 2S_{1/2}$	r	4.10	34.8	34.8	7.33	1.5973	5.3612
$1s2p2s(3P)^2 P_{3/2}^0 - 1s^2 2s^2 2S_{1/2}$	s	10.7	0.29	0.29	1.12	1.5905	5.3947
$1s2p2s(3P)^2 P_{1/2}^0 - 1s^2 2s^2 2S_{1/2}$	t	6.83	32.4	32.4	11.3	1.5911	5.3914
$1s2p2s(3P)^4 P_{3/2}^0 - 1s^2 2s^2 2S_{1/2}$	u	0.13	2.95	2.95	0.51	1.6052	5.3223
$1s2p2s(3P)^4 P_{1/2}^0 - 1s^2 2s^2 2S_{1/2}$	v	0.03	0.81	0.81	0.06	1.6066	5.3164

(b)			
Transitions	λ (Å)	$F_2^*(s)$ (10^{13} sec^{-1})	E_s (keV)
$1s2s3s^2 S_{1/2} - 1s^2 3p^2 P_{3/2}$	1.6018	1.07	6.6867
$1s2p3p^4 D_{5/2} - 1s^2 3p^2 P_{3/2}$	1.5968	2.78	6.7344
$1s2p3d^4 F_{7/2} - 1s^2 3d^2 D_{5/2}$	1.5955	1.14	6.7480
$1s2p3p^2 D_{3/2} - 1s^2 3p^2 P_{3/2}$	1.5952	1.09	6.7418
$1s2p3s^2 P_{1/2} - 1s^2 3s^2 S_{1/2}$	1.5935	5.26	6.7281
$1s2p3p^2 D_{5/2} - 1s^2 3p^2 P_{3/2}$	1.5906	1.58	6.7768
$1s2p3s^2 P_{3/2} - 1s^2 3s^2 S_{1/2}$	1.5895	1.12	6.7478
$1s2p3p^2 D_{5/2} - 1s^2 3p^2 P_{3/2}$	1.5881	15.5	6.7768
$1s2p3p^2 D_{3/2} - 1s^2 3p^2 P_{1/2}$	1.5874	13.0	6.7418
$1s2p3p^2 P_{3/2} - 1s^2 3p^2 P_{3/2}$	1.5872	6.40	6.7565
$1s2p3d^2 D_{5/2} - 1s^2 3d^2 D_{5/2}$	1.5871	1.01	6.7666
$1s2p3s^2 P_{1/2} - 1s^2 3s^2 S_{1/2}$	1.5870	2.40	6.7281
$1s2p3d^2 F_{7/2} - 1s^2 3d^2 D_{5/2}$	1.5868	11.5	6.7747
$1s2p3d^2 D_{5/2} - 1s^2 3d^2 D_{3/2}$	1.5866	1.13	6.7666
$1s2p3p^2 S_{1/2} - 1s^2 3p^2 P_{3/2}$	1.5861	2.91	6.7659
$1s2p3d^2 F_{5/2} - 1s^2 3d^2 D_{5/2}$	1.5860	3.82	6.7524
$1s2p3d^2 F_{5/2} - 1s^2 3d^2 D_{3/2}$	1.5856	3.28	6.7524

TABLE III. (Continued.)

(c)			
Transitions	λ (Å)	$F_2^*(s)$ (10^{13} sec $^{-1}$)	E_s (keV)
$1s2p4p^4D_{5/2}-1s^24p^2P_{3/2}$	1.5950	2.40	7.1949
$1s2p4p^2D_{3/2}-1s^24p^2P_{3/2}$	1.5945	1.59	7.1972
$1s2p4d^4F_{7/2}-1s^24d^2D_{5/2}$	1.5944	0.99	7.2006
$1s2p4s^2P_{1/2}-1s^24s^2S_{1/2}$	1.5940	1.95	7.1903
$1s2p4p^2D_{5/2}-1s^24p^2P_{3/2}$	1.5867	4.23	7.1949
$1s2p4p^2D_{3/2}-1s^24p^2P_{1/2}$	1.5865	4.77	7.1972
$1s2p4p^2P_{3/2}-1s^24p^2P_{3/2}$	1.5865	2.12	7.2368
$1s2p4d^2F_{7/2}-1s^24d^2D_{5/2}$	1.5863	5.38	7.2405
$1s2p4p^2S_{1/2}-1s^24p^2P_{3/2}$	1.5862	1.07	7.2381
$1s2p4d^2D_{5/2}-1s^24d^2D_{3/2}$	1.5861	1.18	7.2404
$1s2p4d^2F_{5/2}-1s^24d^2D_{5/2}$	1.5860	2.12	7.2419
$1s2p4d^2F_{5/2}-1s^24d^2D_{3/2}$	1.5858	1.00	7.2419
(d)			
Transitions	λ (Å)	$F_2^*(s)$ (10^{13} sec $^{-1}$)	E_s (keV)
$1s2p5p^4D_{5/2}-1s^25p^2P_{3/2}$	1.5945	1.17	7.4062
$1s2p5p^2D_{5/2}-1s^25p^2P_{3/2}$	1.5862	2.05	7.4285
$1s2p5p^2D_{3/2}-1s^25p^2P_{1/2}$	1.5861	2.31	7.4074
$1s2p5p^2F_{7/2}-1s^25d^2D_{5/2}$	1.5860	2.77	7.4310
$1s2p5p^2F_{5/2}-1s^25d^2D_{5/2}$	1.5859	1.13	7.4499

TABLE IV. Ni XXVI extrapolation of high- n satellite lines. Numbers in square brackets are powers of ten, e.g., $3.2425[13]=3.2425\times 10^{13}$.

n	odd (o) or even (e) terms	Convergence on w		Convergence on y	
		λ (Å)	$F_2^*(s)$ (sec $^{-1}$)	λ (Å)	$F_2^*(s)$ (sec $^{-1}$)
6	o	1.5858	3.2425[13]	1.5940	1.5396[13]
	e	1.5859	3.7823[13]	1.5943	3.0799[13]
7	o	1.5857	2.0419[13]	1.5941	0.9695[13]
	e	1.5858	2.3819[13]	1.5943	1.9395[13]
≥ 8	o	1.5856	6.2430[13]	1.5941	2.9430[13]
	e	1.5857	7.2303[13]	1.5942	5.5334[13]

TABLE V. (a) Ni XXV $n=2$ strong dielectronic satellite lines (only lines with line factors of 1/100 or larger than the strongest satellite are listed). A_a , A_r , and $F_2^*(s)$ are in units of 10^{13} sec $^{-1}$. The energy E_s of the upper quantum state is relative to the ground state of the lithiumlike ion. An asterisk denotes spectral lines which can also be excited by inner-shell excitation from the ground state of Ni XXV. (b) Ni XXV $n=3$ strong dielectronic satellite lines. (c) Ni XXV $n=4$ dielectronic satellite lines.

Transitions	(a)					λ (Å)	E_s (keV)
	A_a	$\sum A_a$	A_r	$\sum A_r$	$F_2^*(s)$		
$1s2s^22p^3P_2-1s^22p^2^3P_2$	6.99	19.55	0.72	1.41	0.60	1.6382	5.4250
$1s2s2p^2^5P_3-1s^22s2p^3P_2$	1.17	1.34	2.21	2.21	2.55	1.6163	5.4449
$1s2s2p^2^3P_2-1s^22s2p^1P_1$	5.83	12.33	3.61	65.06	0.68	1.6128	5.4998
$1s2s^22p^3P_1-1s^22s^2^1S_0^*$	6.42	18.54	6.00	7.23	2.25	1.6097	5.4050
$1s2s2p^2^3P_1-1s^22s2p^3P_2$	5.16	6.46	14.23	77.08	1.32	1.6088	5.4806
$1s2s2p^2^1D_2-1s^22s2p^1P_1$	9.57	20.71	18.03	40.37	7.06	1.6087	5.5194
$1s2s2p^2^3D_2-1s^22s2p^3P_2$	12.65	14.52	3.66	50.00	1.79	1.6081	5.4840
$1s2s2p^2^3D_3-1s^22s2p^3P_2$	15.88	18.13	30.54	30.54	34.88	1.6064	5.4925
$1s2s2p^2^3P_2-1s^22s2p^1P_1$	5.89	23.66	11.44	11.58	4.78	1.6055	5.4998
$1s2s2p^2^3P_2-1s^22s2p^3P_2$	5.83	12.33	57.50	65.06	10.83	1.6048	5.4998
$1s2s2p^2^3P_1-1s^22s2p^3P_1$	5.16	6.46	8.20	77.08	0.76	1.6048	5.4806
$1s2s2p^2^3D_2-1s^22s2p^3P_1$	12.65	14.52	45.34	50.00	22.23	1.6040	5.4840
$1s2s2p^2^3P_1-1s^22s2p^3P_2$	2.37	15.12	9.06	17.83	0.98	1.6037	5.4732
$1s2s2p^2^3P_1-1s^22s2p^3P_0$	5.16	6.46	54.64	77.08	5.06	1.6035	5.4732
$1s2s2p^2^3D_1-1s^22s2p^3P_1$	11.59	15.00	37.97	48.45	10.40	1.6029	5.4895
$1s2s2p^2^1P_1-1s^22s2p^1P_1$	0.68	7.80	93.73	94.14	0.94	1.6029	5.4773
$1s2s2p^2^1S_0-1s^22s2p^1P_1$	6.37	21.89	31.73	31.76	1.88	1.6015	5.5540
$1s2s^22p^1P_1-1s^22s^2^1S_0^*$ (b)	0.77	13.60	60.41	62.61	0.91	1.6015	5.4474

TABLE V. (Continued.)

(a)							
Transitions	A_a	$\sum A_a$	A_r	$\sum A_r$	$F_2^*(s)$	λ (Å)	E_s (keV)
$1s2s2p^2\ ^3P_2 - 1s^22s2p\ ^3P_1$	5.83	12.33	3.95	65.06	0.74	1.6008	5.4998
$1s2s2p^2\ ^1D_2 - 1s^22s2p\ ^3P_2$	9.57	20.71	22.28	40.37	8.73	1.6008	5.5194
$1s2s2p^2\ ^3P_1 - 1s^22s2p\ ^3P_1$	2.37	15.12	4.83	17.83	0.52	1.5997	5.4732
$1s2s2p^2\ ^3S_1 - 1s^22s2p\ ^3P_2$	3.92	11.00	29.05	29.65	4.20	1.5992	5.5268
(b)							
Transitions	λ (Å)			$F_2^*(s)$ ($10^{12}\ \text{sec}^{-1}$)			
$1s2s2p3p\ ^5D_3 - 1s^22s3p\ ^3P_2$	1.6085			6.11	6.6948		
$1s2p^23s\ ^5P_3 - 1s^22p3s\ ^3P_2$	1.6070			5.61	6.7540		
$1s2s2p3p\ ^3D_1 - 1s^22s3p\ ^1P_1$	1.6064			7.88	6.7030		
$1s2s2p3s\ ^3P_1 - 1s^22s3s\ ^1S_0$	1.6060			7.59	6.7331		
$1s2s2p3p\ ^1D_2 - 1s^22p3s\ ^1P_1$	1.6051			8.14	6.7466		
$1s2s2p3p\ ^3D_2 - 1s^22s3p\ ^3P_1$	1.5999			9.12	6.7356		
$1s2s2p3p\ ^3D_2 - 1s^22s3p\ ^1P_1$	1.5997			8.95	6.7365		
$1s2s2p3d\ ^3F_3 - 1s^22s3d\ ^3D_3$	1.5979			9.45	6.8055		
$1s2s2p3d\ ^3F_3 - 1s^22s3d\ ^3D_2$	1.5976			5.86	6.8055		
$1s2s2p3p\ ^3D_3 - 1s^22s3p\ ^3P_2$	1.5969			60.85	6.7501		
$1s2s2p3p\ ^3S_1 - 1s^22s3p\ ^1P_1$	1.5963			6.35	6.7520		
$1s2s2p3p\ ^1D_2 - 1s^22s3p\ ^3P_1$	1.5960			62.17	6.7466		
$1s2s2p3d\ ^1F_3 - 1s^22s3d\ ^1D_2$	1.5960			25.55	6.8239		
$1s2s2p3d\ ^3F_4 - 1s^22s3d\ ^3D_3$	1.5953			63.06	6.7926		
$1s2s2p3d\ ^3D_3 - 1s^22s3d\ ^3D_2$	1.5952			6.86	6.7867		
$1s2s2p3p\ ^3D_2 - 1s^22s3p\ ^3P_2$	1.5944			26.37	6.7620		
$1s2s2p3p\ ^3D_2 - 1s^22s3p\ ^1P_1$	1.5943			10.82	6.7620		
$1s2s2p3p\ ^3D_1 - 1s^22s3p\ ^3P_1$	1.5934			23.39	6.7030		
$1s2s2p3p\ ^3D_1 - 1s^22s3p\ ^3P_0$	1.5934			10.90	6.7030		
$1s2s2p3p\ ^1D_2 - 1s^22s3p\ ^3P_2$	1.5927			12.39	6.7466		
$1s2s2p3p\ ^3P_1 - 1s^22s3p\ ^3P_2$	1.5925			6.45	6.7457		
(c)							
Transitions	λ (Å)			$F_2^*(s)$ ($10^{12}\ \text{sec}^{-1}$)			
$1s2s2p4p\ ^5D_3 - 1s^22s4p\ ^3P_2$	1.6063			8.33	7.1301		
$1s2s2p4p\ ^3D_2 - 1s^22s4p\ ^1P_1$	1.5982			7.71	7.1328		
$1s2s2p4p\ ^3D_2 - 1s^22s4p\ ^3P_2$	1.5981			8.87	7.1328		
$1s2s2p4d\ ^3F_3 - 1s^22s4d\ ^3D_3$	1.5975			5.38	7.2256		
$1s2s2p4p\ ^3D_3 - 1s^22s4p\ ^3P_2$	1.5951			26.61	7.1503		
$1s2s2p4p\ ^3P_2 - 1s^22s4p\ ^1P_1$	1.5950			6.30	7.1486		
$1s2s2p4p\ ^1D_2 - 1s^22s4p\ ^3P_1$	1.5949			12.62	7.1827		
$1s2s2p4p\ ^3P_2 - 1s^22s4p\ ^3P_2$	1.5949			5.67	7.1486		
$1s2s2p4d\ ^1F_3 - 1s^22s4d\ ^1D_2$	1.5947			16.36	7.2596		
$1s2s2p4d\ ^3F_4 - 1s^22s4d\ ^3D_3$	1.5946			31.20	7.2396		
$1s2s2p4d\ ^3D_3 - 1s^22s4d\ ^3D_2$	1.5945			5.56	7.2395		
$1s2s2p4p\ ^3D_1 - 1s^22s4p\ ^3P_1$	1.5919			6.42	7.1970		

TABLE VI. Ni XXIV $n=2$ strong dielectronic satellite lines (only lines with line factors of 1/100 or larger than the strongest satellite line are listed). A_a , A_r , and $F_2^*(s)$ are in units of $10^{13}\ \text{sec}^{-1}$. The energy E_s of the upper quantum state is related to the ground state of the berylliumlike ion. The letters *A, B, C* designate lines discussed in the text.

Transitions	A_a	$\sum A_a$	A_r	$\sum A_r$	$F_2^*(s)$	λ (Å)	E_s (keV)
$1s2s^22p^2\ ^2D_{5/2} - 1s^22p^3\ ^2D_{5/2}$	13.68	37.65	0.62	27.51	0.79	1.6550	5.8912
$1s2s^22p^2\ ^4P_{1/2} - 1s^22s^22p\ ^2P_{1/2}$	1.18	26.08	6.16	68.63	0.44	1.6208	5.8369
$1s2s^22p^2\ ^4P_{5/2} - 1s^22s^22p\ ^2P_{3/2}$	3.03	28.39	5.76	6.35	3.01	1.6205	5.8609
$1s2s^22p^2\ ^2P_{1/2} - 1s^22s^22p\ ^2P_{3/2}$	1.22	18.27	13.12	86.56	0.30	1.6165	5.8797
$1s2s^22p^2\ ^2D_{3/2} - 1s^22s^22p\ ^2P_{3/2}$	12.80	34.25	5.44	49.08	3.34	1.6165	5.8801
$1s2s^22p^2\ ^2D_{5/2} - 1s^22s^22p\ ^2P_{3/2}$ <i>C</i>	13.68	37.65	26.57	27.51	33.47	1.6141	5.8912
$1s2s^22p^2\ ^2P_{1/2} - 1s^22s^22p\ ^2P_{1/2}$ <i>B</i>	1.22	18.27	72.02	86.56	1.67	1.6118	5.8797
$1s2s^22p^2\ ^2D_{3/2} - 1s^22s^22p\ ^2P_{1/2}$ <i>A</i>	12.80	34.25	42.71	49.08	26.24	1.6117	5.8801
$1s2s^22p^2\ ^2P_{3/2} - 1s^22s^22p\ ^2P_{3/2}$	3.72	21.70	82.01	84.75	11.46	1.6109	5.9067
$1s2s^22p^2\ ^2S_{1/2} - 1s^22s^22p\ ^2P_{3/2}$	9.18	30.29	42.98	44.16	10.60	1.6097	5.9125

TABLE VII. Inner-shell excitation rate coefficients C ($\text{cm}^3 \text{sec}^{-1}$) from the ground state $1s^2 2s^2 S_{1/2}$ of Ni XXVI. $1s2s2p^4 P_{5/2}$ branching ratio is 0.58, extrapolated from Ref. 44, wavelength is $\lambda = 1.6017 \text{ \AA}$. Numbers in square brackets are powers of ten, e.g., $0.348[-17] = 0.348 \times 10^{-17}$.

T_e (keV)	$1s2s^2 S_{1/2}(o)$	$1s2s2p^4 P_{1/2}(v)$	$1s2s2p^4 P_{3/2}(u)$	$1s2s2p^2 P_{1/2}(r)$
0.6	0.348[-17]	0.174[-17]	0.341[-17]	0.396[-17]
1.0	0.460[-15]	0.217[-15]	0.436[-15]	0.569[-15]
1.4	0.353[-14]	0.158[-14]	0.323[-14]	0.462[-14]
1.8	0.106[-13]	0.452[-14]	0.943[-14]	0.146[-13]
2.2	0.210[-13]	0.855[-14]	0.181[-13]	0.300[-13]
2.6	0.332[-13]	0.130[-13]	0.279[-13]	0.492[-13]
3.0	0.460[-13]	0.173[-13]	0.379[-13]	0.706[-13]
3.4	0.586[-13]	0.213[-13]	0.473[-13]	0.927[-13]
3.8	0.705[-13]	0.247[-13]	0.559[-13]	0.115[-12]
4.2	0.816[-13]	0.277[-13]	0.635[-13]	0.136[-12]
4.6	0.917[-13]	0.302[-13]	0.703[-13]	0.157[-12]
5.0	0.101[-12]	0.323[-13]	0.762[-13]	0.177[-12]
6.0	0.120[-12]	0.359[-13]	0.878[-13]	0.222[-12]
T_e (keV)	$1s2s2p^2 P_{3/2}(q)$	$1s2s2p^2 P_{1/2}(t)$	$1s2s2p^2 P_{3/2}(s)$	$1s2s2p^4 P_{5/2}$
0.6	0.110[-16]	0.320[-17]	0.280[-17]	0.432[-17]
1.0	0.164[-14]	0.467[-15]	0.369[-15]	0.645[-15]
1.4	0.136[-13]	0.382[-14]	0.274[-14]	0.397[-14]
1.8	0.438[-13]	0.121[-13]	0.794[-14]	0.114[-13]
2.2	0.915[-13]	0.249[-13]	0.151[-13]	0.214[-13]
2.6	0.152[-12]	0.410[-13]	0.229[-13]	0.324[-13]
3.0	0.220[-12]	0.589[-13]	0.306[-13]	0.431[-13]
3.4	0.292[-12]	0.775[-13]	0.376[-13]	0.528[-13]
3.8	0.365[-12]	0.962[-13]	0.437[-13]	0.611[-13]
4.2	0.436[-12]	0.114[-12]	0.489[-13]	0.682[-13]
4.6	0.506[-12]	0.132[-12]	0.532[-13]	0.740[-13]
5.0	0.572[-12]	0.149[-12]	0.567[-13]	0.786[-13]
6.0	0.725[-12]	0.187[-12]	0.626[-13]	0.862[-13]

4. Inner-shell satellites

The alternative method for exciting satellite lines is the excitation of an inner-shell electron by electron impact. This process is important only for $n=2$ satellites

in the spectral range considered and requires the calculation of the appropriate excitation rates. The excitation rate coefficients are given in Table VII for the lithium-like Ni XXVI ion. These must be multiplied by the autoionizing level branching ratio

TABLE VIII. Inner-shell excitation rate coefficients C ($\text{cm}^3 \text{sec}^{-1}$) from the ground state to the $1s2s^2 2p^2$ states as indicated. Spectral lines corresponding to A, B, C are discussed in the text. Numbers in square brackets are powers of ten, e.g., $0.319[-17] = 0.319 \times 10^{-17}$.

T_e (keV)	Direct excitation				Two-stage excitation	
	$^4 P_{1/2}$	$1s^2 2s^2 2p^2 P_{1/2} - 1s2s^2 2p^2$ $^2 D_{3/2} (A)$	$^2 P_{1/2} (B)$	$^2 P_{3/2}$	$1s^2 2s^2 2p^2 P_{1/2} - 1s^2 2s^2 2p^2 P_{3/2}^a$	$1s^2 2s^2 2p^2 P_{3/2} - 1s2s^2 2p^2 D_{5/2} (C)$
0.6	0.319[-17]	0.888[-17]	0.661[-17]	0.316[-18]	0.380[-10]	0.702[-17]
1.0	0.388[-15]	0.123[-14]	0.927[-15]	0.428[-16]	0.288[-10]	0.920[-15]
1.4	0.282[-14]	0.991[-14]	0.754[-14]	0.335[-15]	0.214[-10]	0.709[-14]
1.8	0.814[-14]	0.312[-13]	0.239[-13]	0.103[-14]	0.178[-10]	0.215[-13]
2.2	0.156[-13]	0.642[-13]	0.496[-13]	0.207[-14]	0.155[-10]	0.430[-13]
2.6	0.240[-13]	0.106[-12]	0.822[-13]	0.333[-14]	0.136[-10]	0.688[-13]
3.0	0.324[-13]	0.152[-12]	0.119[-12]	0.470[-14]	0.122[-10]	0.966[-13]
3.4	0.405[-13]	0.200[-12]	0.157[-12]	0.609[-14]	0.111[-10]	0.125[-12]
3.8	0.478[-13]	0.249[-12]	0.196[-12]	0.745[-14]	0.103[-10]	0.152[-12]
4.2	0.544[-13]	0.296[-12]	0.235[-12]	0.877[-14]	0.944[-11]	0.179[-12]
4.6	0.603[-13]	0.343[-12]	0.272[-12]	0.100[-13]	0.871[-11]	0.204[-12]
5.0	0.654[-13]	0.387[-12]	0.308[-12]	0.112[-13]	0.822[-11]	0.227[-12]
6.0	0.756[-13]	0.488[-12]	0.391[-12]	0.138[-13]	0.719[-11]	0.278[-12]

^aThe rate coefficients of this column are extrapolated from results for iron given by Mason and Storey, Ref. 25. The radiative probability of the corresponding line is $5.55 \times 10^4 \text{ sec}^{-1}$ (magnetic dipole).

$$\frac{A_r}{\sum A_a + \sum A_r}$$

obtained from Table III(a) in order to derive line emissivities (radiative cascades between autoionizing levels are negligible).

In the case of the berylliumlike ions, inner-shell excitation efficiently excites only two of the levels; those marked with an asterisk in Table V(a). The excitation of these levels is a process similar to the excitation of the line intensities w and y in the He-like ion. Detailed calculations for iron have shown that the screening effect due to the closed $2s^2$ shell reduces the corresponding excitation rate by only a few percent. The emissivity of the $1s^2 2s^2 - 1s 2s^2 2p^1 P_1$ line (called β in the literature) and the $1s^2 2s^2 - 1s 2s^2 2p^3 P_1$ line can therefore be estimated from the values given for w and y in Table I column (a) multiplied by the branching ratio $A_r / (\sum A_a + \sum A_r)$ obtained from Table V(a). The effect of the branching ratio is to cause the β line to be strong and the other line weak.

For the five-electron spectrum of boronlike Ni XXIV the excitation rates for inner-shell excitation are given in Table VIII. The rate coefficients for the first excitation in a possible two-stage excitation process are extrapolated from results for iron given by Mason and Storey.²⁵ To obtain intensities, the excitation rates must be multiplied by the branching ratios derived from Table VI, the density of boronlike ions, and the electron density.

B. Hydrogenlike spectrum

The wavelengths of the hydrogenlike nickel Lyman- α doublet lines (Lyman- α_1 $2p^2 P_{3/2} - 1s^2 S_{1/2}$ and Lyman- α_2 $2p^2 P_{1/2} - 1s^2 S_{1/2}$) are, respectively, 1.5297 Å and 1.5350 Å (these values do not include quantum electrodynamics effects, see Mohr²⁶). Excitation rates for H-like Ni has been extrapolated from the results on Ca (Ref. 27) using a Z scaling. Using the collisional radiative code described by Tallents,²⁸ the intensity ratio of the Lyman- α_2 to Lyman- α_1 lines can be shown to be in the ratio (0.5) of the statistical weights of the upper quantum states and the magnetic dipole line ($2s^2 S_{1/2} - 1s^2 S_{1/2}$) at 1.53486 Å (including a Lamb shift of 1.4×10^{-4} Å) can be shown to have 5% of the intensity of the Lyman- α_1 component.

The wavelengths and intensities of the heliumlike dielectronic satellites are evaluated using the SUPERSTRUCTURE program as outlined in Sec. III A. Table IX(a) gives the Ni XXVII $n=2$ dielectronic satellite wavelengths $F_2^*(s)$ and E_s values obtained by diagonalization of a large basis set including all configurations with $n=2, 3, 4, 5$ orbitals (i.e., 42 configurations). Data from the same computation for $n=3, 4$, and 5 are given in Tables IX(b), IX(c), and IX(d). The mono-electronic wave functions used in the calculations are hydrogenic. Direct excitation of the heliumlike ground state cannot produce dielectronic satellites with any reasonable probability as it would be necessary to excite two electrons

TABLE IX. (a) Ni XXVII $n=2$ dielectronic satellite lines. The energy E_s of the upper quantum state is relative to the ground state of the hydrogenlike ion. (b) Ni XXVII $n=3$ strong dielectronic satellites. (c) Ni XXVII $n=4$ strong dielectronic satellites. (d) Ni XXVII $n=5$ strong dielectronic satellites (only lines with line factors of 1/100 or larger than the strongest satellite are listed).

Transitions	λ (Å)	$F_2^*(s)$ (10^{13} sec^{-1})	E_s (keV)
(a)			
$2s^2 1S_0 - 1s 2p^1 P_1$	1.5583	2.20	5.4742
$2s^2 1S_0 - 1s 2p^3 P_1$	1.5500	2.81	5.4742
$2s^2 3P_2 - 1s 2p^1 P_1$	1.5461	6.23	5.5369
$2s 2p^3 P_0 - 1s 2s^3 S_1$	1.5430	0.59	5.4774
$2p^2 3P_2 - 1s 2p^3 S_2$	1.5423	13.66	5.5369
$2s 2p^3 P_1 - 1s 2s^3 S_1$	1.5418	2.87	5.4836
$2p^2 1D_2 - 1s 2p^1 P_1$	1.5409	30.26	5.5637
$2p^2 3P_2 - 1s 2p^3 P_1$	1.5380	9.49	5.5369
$2s 2p^3 P_2 - 1s 2s^3 S_1$	1.5377	2.90	5.5052
$2p^2 1D_2 - 1s 2p^3 P_2$	1.5371	12.33	5.5637
$2s 2p^1 P_1 - 1s 2s^1 S_0$	1.5366	17.00	5.5431
$2p^2 1S_0 - 1s 2p^1 P_1$	1.5340	2.14	5.6001
$2s 2p^1 P_1 - 1s 2s^3 S_1$	1.5305	0.91	5.5431
(b)			
$2s 3s^1 S_0 - 1s 3p^1 P_1$	1.5409	0.89	6.9421
$2s 3p^3 P_2 - 1s 3d^3 D_3$	1.5393	0.31	6.9520
$2p 3p^3 D_2 - 1s 3p^1 P_1$	1.5386	0.78	6.9543
$2s 3s^1 S_0 - 1s 3p^3 P_1$	1.5385	1.72	6.9421
$2p 3p^3 D_2 - 1s 3p^3 P_2$	1.5375	1.27	6.9543
$2p 3d^3 F_2 - 1s 3d^3 D_2$	1.5374	0.44	6.9594
$2p 3d^3 F_2 - 1s 3d^3 D_1$	1.5374	0.54	6.9594
$2s 3d^3 D_2 - 1s 3p^1 P_1$	1.5368	1.53	6.9638

TABLE IX. (Continued.)

Transitions	λ (Å)	(b) F_2^* (s) (10^{13} sec $^{-1}$)	E_r (keV)
$2p3d\ ^3F_3-1s3d\ ^3D_3$	1.5363	0.95	6.9678
$2p3p\ ^3D_2-1s3p\ ^3P_1$	1.5362	0.62	6.9543
$2s3p\ ^3P_1-1s3s\ ^3S_1$	1.5360	0.64	6.9457
$2s3d\ ^3D_2-1s3p\ ^3P_2$	1.5357	1.30	6.9638
$2p3s\ ^3P_1-1s3s\ ^3S_1$	1.5341	1.32	6.9559
$2s3d\ ^1D_2-1s3p\ ^3P_1$	1.5328	1.21	6.9731
$2p3p\ ^3P_2-1s3p\ ^3P_2$	1.5322	1.05	6.9821
$2p3d\ ^3F_4-1s3d\ ^3D_3$	1.5321	2.28	6.9895
$2p3p\ ^1D_2-1s3p\ ^1P_1$	1.5311	10.83	6.9901
$2p3p\ ^3P_2-1s3p\ ^3P_1$	1.5309	3.12	6.9821
$2p3s\ ^1P_1-1s3s\ ^1S_0$	1.5309	6.26	6.9816
$2p3p\ ^1D_2-1s3p\ ^3P_2$	1.5300	4.91	6.9938
$2p3s\ ^1P_1-1s3s\ ^3S_1$	1.5292	1.31	6.9816
$2p3d\ ^1F_3-1s3d\ ^3D_3$	1.5290	1.00	7.0063
$2p3d\ ^1F_3-1s3d\ ^1D_2$	1.5290	2.80	7.0063
$2p3p\ ^1S_0-1s3p\ ^1P_1$	1.5287	1.01	7.0063
$2p3d\ ^1F_3-1s3d\ ^3D_2$	1.5285	1.73	7.0068
(c)			
$2s4s\ ^1S_0-1s4p\ ^1P_1$	1.5376	0.32	7.4433
$2s4s\ ^1S_0-1s4p\ ^3P_1$	1.5365	1.33	7.4433
$2p4p\ ^3D_2-1s4p\ ^1P_1$	1.5364	1.16	7.4494
$2p4p\ ^3D_2-1s4p\ ^3P_2$	1.5359	1.44	7.4512
$2s4d\ ^3D_2-1s4p\ ^1P_1$	1.5357	0.43	7.4531
$2s4d\ ^3D_2-1s4p\ ^3P_2$	1.5352	0.34	7.4531
$2s4p\ ^1P_1-1s4s\ ^3S_0$	1.5342	1.37	7.4528
$2s4d\ ^3F_4-1s4d\ ^3D_3$	1.5306	1.23	7.4804
$2p4s\ ^1P_1-1s4s\ ^1S_0$	1.5306	1.82	7.4743
$2p4p\ ^1D_2-1s4p\ ^1P_1$	1.5306	4.14	7.4805
$2p4p\ ^3P_2-1s4p\ ^3P_1$	1.5304	3.00	7.4754
$2p4d\ ^3D_3-1s4d\ ^3D_2$	1.5302	0.47	7.4813
$2p4p\ ^1D_2-1s4p\ ^3P_2$	1.5300	3.10	7.4805
$2p4s\ ^1P_1-1s4s\ ^3S_1$	1.5299	0.73	7.4743
$2p4d\ ^1F_3-1s4d\ ^3D_3$	1.5296	0.92	7.4858
$2p4d\ ^1F_3-1s4d\ ^1D_2$	1.5296	1.31	7.4858
$2p4p\ ^1S_0-1s4p\ ^1P_1$	1.5296	0.67	7.4851
$2p4d\ ^1F_3-1s4d\ ^3D_2$	1.5294	0.82	7.4858
(d)			
$2p5p\ ^1D_2-1s5p\ ^1P_1$	1.5344	0.93	7.6773
$2s5s\ ^1S_0-1s5p\ ^3P_1$	1.5358	0.92	7.6738
$2p5p\ ^1D_2-1s5p\ ^3P_2$	1.5355	1.07	7.6773
$2p5d\ ^3F_3-1s5d\ ^3D_3$	1.5353	0.41	7.6803
$2p5d\ ^3F_3-1s5d\ ^1D_2$	1.5353	0.46	7.6803
$2s5p\ ^1P_1-1s5s\ ^3S_1$	1.5344	0.91	7.6788
$2p5s\ ^1P_1-1s5s\ ^1S_0$	1.5303	0.83	7.7030
$2p5d\ ^3F_4-1s5d\ ^3D_3$	1.5302	0.79	7.7068
$2p5p\ ^3P_2-1s5p\ ^1P_1$	1.5302	2.31	7.7067
$2p5p\ ^3D_2-1s5p\ ^3P_1$	1.5301	1.89	7.7038
$2p5d\ ^3D_3-1s5d\ ^3D_2$	1.5300	0.35	7.7072
$2p5p\ ^3P_2-1s5p\ ^3P_2$	1.5300	1.96	7.7067
$2p5s\ ^1P_1-1s5s\ ^3S_1$	1.5299	0.38	7.7030
$2p5p\ ^1S_0-1s5p\ ^1P_1$	1.5298	0.48	7.7092
$2p5d\ ^1F_3-1s5d\ ^3D_3$	1.5297	0.70	7.7097
$2p5d\ ^1F_3-1s5d\ ^1D_2$	1.5297	0.83	7.7097
$2p5d\ ^1F_3-1s5d\ ^3D_2$	1.5296	0.52	7.7097

together. The intensities of the satellites to the hydrogenlike lines can, therefore, be found in a straightforward manner, using the $F_2^*(s)$ and E_s values of Table IX and Eq. (3).

IV. SIMULATION OF THE SPECTRA

The experimentally observed spectra presented in Sec. II have been simulated by integrating theoretical spectra derived from the data of Sec. III along the spectrograph line of sight. The radial electron temperature and density variations are measured by other diagnostics on JET and are used to calculate the emissivity at points along the line of sight.

As an example of the He-like spectrum at a particular position in the plasma, the calculated relative emissivities of the satellite lines to the resonance line emitted at the plasma center (i.e., the magnetic axis) are shown in Fig. 3. The wavelengths and emissivities of 148 lines making up the spectrum are considered. The populations of the different ion stages are taken to be in coronal equilibrium with relative values calculated using the data of Ref. 29. The solid curve of Fig. 3 is obtained by summing up the contributions from all lines assuming thermal Doppler (Gaussian) line broadening with an ion temperature equal to the value deduced by fitting a Voigt profile to the experimentally measured resonance line profile (see Sec. II).

The brightness $B(\lambda)$ at wavelength λ seen by the x-ray spectrograph is given by

$$B(\lambda) = \frac{2}{4\pi} \int_{R_0}^{R_1} \frac{\epsilon_{\text{res}} \phi W(\lambda')}{[1 - (R_0/R)^2]^{1/2}} dR, \quad (4)$$

where the integration is with respect to the major radius R , the "impact parameter" $R_0 = 1.82$ m is the distance of closest approach of the line of sight to the center of the torus and $R_1 \simeq 4.2$ m is the outer boundary of the plasma. Other parameters introduced in Eq. (4) are the emissivity of the resonance line ϵ_{res} , a "shape factor" ϕ relating the peak emissivity of the resonance line to the total emissivity ϵ_{res} of the line and the intensity $W(\lambda)$ at wavelength λ of the spectrum relative to the resonance line peak emissivity. For thermal Doppler broadening, the shape factor can be related to the ion temperature T_i in keV and ion atomic weight M in amu by

$$\phi = 390 \lambda_0^{-1} \sqrt{M/T_i}, \quad (5)$$

where λ_0 is the resonance line wavelength.

We set $\lambda' = \lambda \{1 - [v(R)/c](R_0/R)\}$ in order to take account of any bulk plasma motion [of toroidal velocity $v(R)$] producing a Doppler shift of the spectrum. Here the velocity of light is designated by c . However, for the discharges discussed in this paper, $v(R) < 10^4$ m/s and $\lambda' = \lambda$.

In order to perform the integration along the line of sight [Eq. (4)], electron temperatures $T_e(R)$ are obtained from absolutely measured values of the electron cyclotron emission³⁰ and electron densities $N_e(R)$ from interferometric measurements.³¹ Figure 4 shows the calculat-

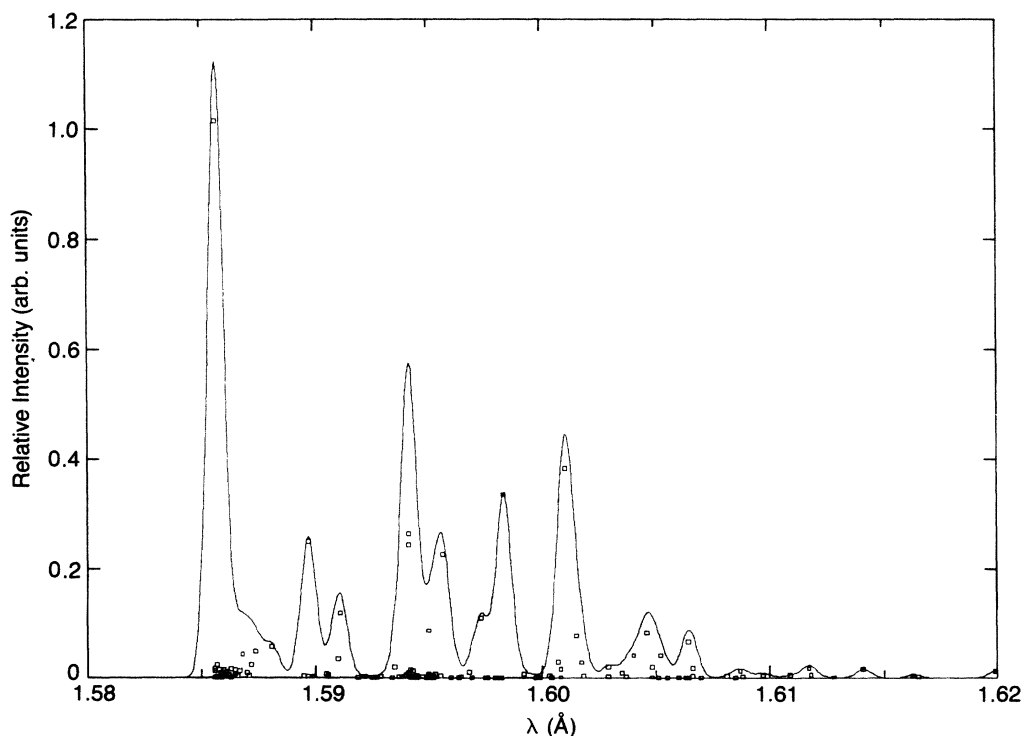


FIG. 3. Calculated relative spectral emissivities near the heliumlike nickel resonance line for an assumed isothermal plasma with conditions found in the plasma center for the experimental spectra of Fig. 2 ($T_e = 2.8$ keV). Coronal ionization balance calculated using the data of Ref. 28 is assumed. The circles show the wavelengths and relative intensities of individual spectral lines.

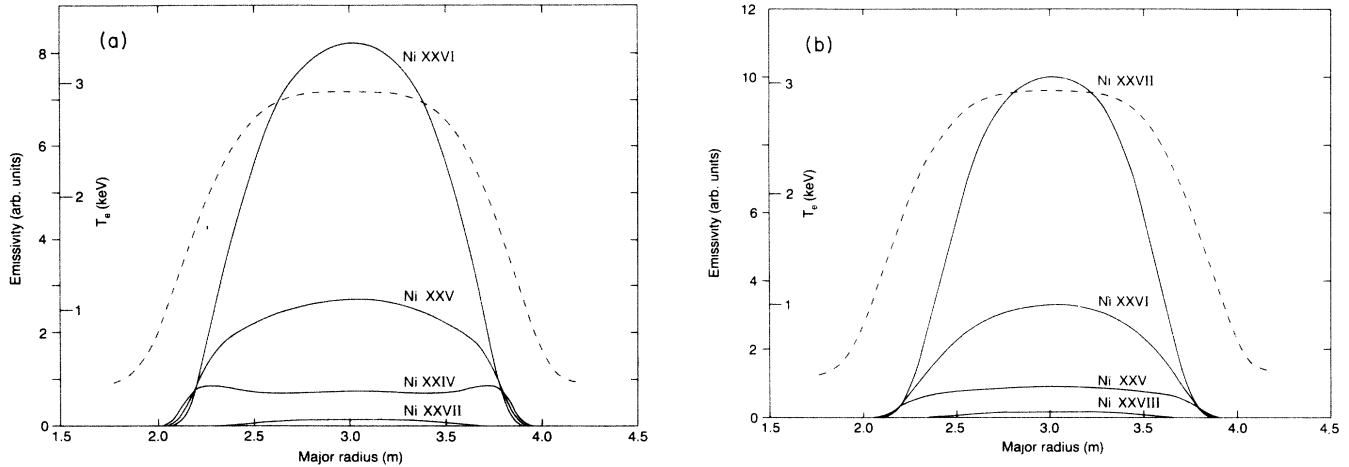


FIG. 4. Calculated emissivities (in arbitrary units) as a function of JET major radius of different nickel ionization stages for the experimental spectra of Fig. 2(a) (peak $T_e = 2.8$ keV). The coronal ionization balance calculated using the data of Ref. 29 is assumed. (a) Spectral lines produced by collisional excitation. (b) Spectral lines produced by dielectronic recombination. The relative magnitudes of the emissivities between different ionization stages are arbitrary. (For clarity of display the values for Ni XXIV [in (a)] are shown greater compared to the other ionization stages.) The profile of the electron temperature variation ($T_e(R) = (2.8 - 0.5) \{ 1 - [(R - 3) / 1.14]^{3.85} \}^{2.97} + 0.5$ (keV)) is shown as a broken line. The shape of the electron density profile ($N_e(R) = (2 - 0.16) \times 10^{13} \{ 1 - [(R - 3) / 1.14]^2 \}^{0.75} + 0.16 \times 10^{13}$ (cm $^{-3}$)) is similar to the electron temperature profile.

ed emissivity of hydrogenlike to boronlike nickel ionization stages for emission caused by collisional excitation [Fig. 4(a)] and dielectronic recombination [Fig. 4(b)] for the plasma conditions of Fig. 2(a) (peak electron temper-

ature 2.8 keV), assuming coronal ionization equilibrium populations obtained using ionization rates from Burgess and Chidichimo,^{29(a)} radiative recombination rates from von Goeler *et al.*^{29(b)} and dielectronic recombination

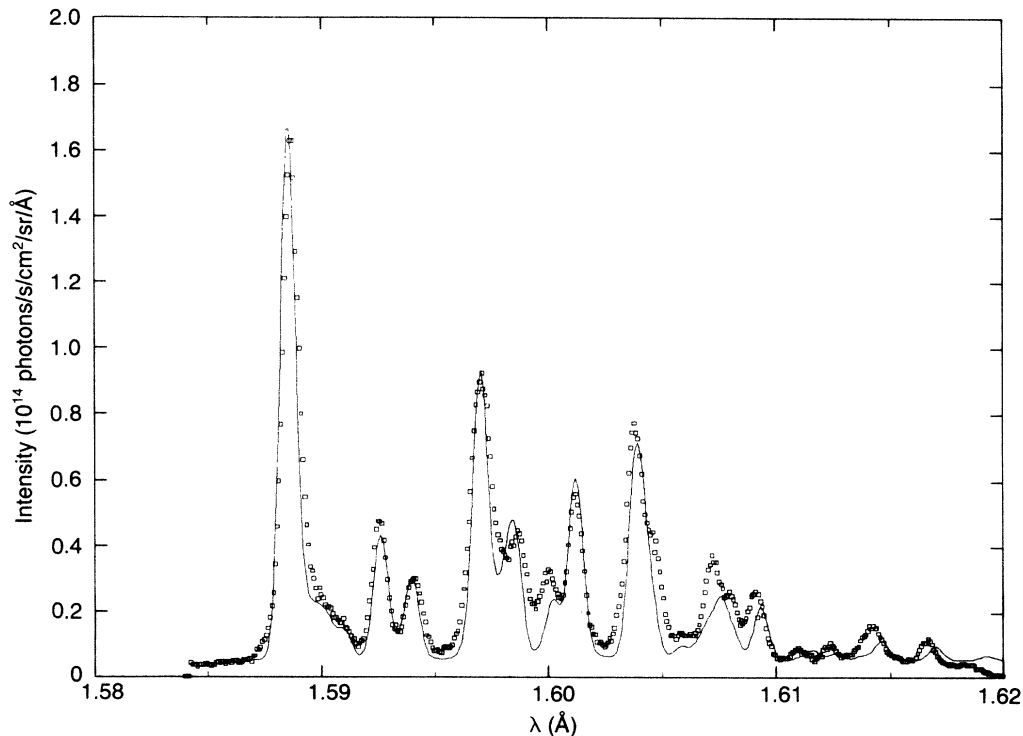


FIG. 5. The simulated heliumlike nickel spectrum and satellites obtained by integrating along the line of sight of the spectrometer (solid line) fitted to the experimentally observed spectrum (data points). Coronal ionization equilibrium data are calculated using the data of Ref. 28 with the peak electron temperature $T_e = 2.8$ keV. Gaussian line profiles with a width corresponding to an ion temperature of 2.39 keV have been used. The data from Fig. 2(a) has been normalized to overlapping peak areas with normalization factors of 1.0299, 0.9770, 0.9025, and 0.7892 for the four joining points.

rates from Post *et al.*^{29(c)} It is assumed that the concentration of nickel varies spatially with the same profile as the electron density.

An example of heliumlike simulated spectra integrated along the line of sight of the x-ray spectrograph is shown in Fig. 5 for a peak electron temperature of 2.8 keV. The relative intensities of the spectral lines of Fig. 5 are almost identical to those shown in Fig. 3 for an isothermal plasma of electron temperature 2.8 keV, illustrating the domination of the spectrum by emission from the central plasma.

V. DISCUSSION

A. Heliumlike spectrum

Parameters in the simulated spectrum (Fig. 5) which are adjusted to optimize the fits to the experimentally recorded spectrum are the level of continuum emission and background, the fraction of nickel in the plasma, and a wavelength shift of all lines. The required shift of the lines is $\approx +2.9$ mÅ and is needed partly because of uncertainties in the absolute determination of the recorded wavelengths (see Sec. II) and partly because of uncertainties in the calculated absolute wavelengths. The experimentally determined wavelengths are listed and compared with calculations from this paper and various authors in Table X. Small shifts of the calculated wavelengths were introduced to obtain the best fit (Fig. 6). In particular, the lines *y* and *q* have been separated by 0.6 mÅ. The experimentally determined wavelengths of the *t* and *k* satellites have been adjusted for the presence of nearby moderately intense satellites (*m* and *a*, respectively) by corrections of +0.024 and +0.073 mÅ estimated from the calculations for Fig. 3.

The theoretical calculations of Sec. III have been made with the same mono-electronic wave functions for the 2–5-electron ions. This ensures good relative wavelengths between ionization stages (see Fig. 5), but may lead to the absolute wavelengths being in error, as the results of Table X suggest. If a wavelength shift of +2.9 mÅ is added to all the wavelengths, we find overall good agreement between the experimental and different theoretical wavelengths,^{32–34} both relative and absolute, within the experimental errors.

The intensities calculated from the theoretical computations of Sec. III and the experimentally observed intensities are in overall approximate agreement (see Fig. 5). The purely dielectronic satellite lines *k* and *j* are best fitted with a peak electron temperature $T_e = 2.8$ keV rather than the peak $T_e = 3.1$ keV measured from electron cyclotron emission.³⁰ However, in Fig. 5, the largest discrepancies between the simulated and observed spectrum arise with the intensities of the berylliumlike and boronlike lines (found at $\lambda > 1.605$ Å in Fig. 5) which, being less ionized than heliumlike and lithiumlike ions, are abundant for lower temperatures and are therefore more sensitive to physical conditions in cooler plasma regions.

The intensities of the three boronlike lines marked *A*, *B*, and *C* in Tables VI and VIII can be used to determine the ratio of the boronlike to berylliumlike populations. The three lines give rise to two peaks clearly seen in Fig. 2(a) spectrum at wavelengths 1.6144 and 1.6167 Å (*A* and *B* are blended as a single feature). From the atomic data of Table VI, the dielectronic intensities through recombination of the Be-like ion are in the ratio $(A + B)/C = 0.83$, while the observed spectrum shows a

TABLE X. Experimentally determined wavelengths and various theoretical wavelength calculations. Where possible spectral lines are designated by symbols discussed in the text. The relative accuracy of the experimental wavelengths is approximately ± 0.0001 Å. The absolute accuracy of the experimental wavelengths is approximately ± 0.001 Å.

Line	Wavelengths (Å)					
	This work (experimental)	This work (theoretical)	This work (theory) plus 0.0029 Å	Ref. 32	Ref. 33	Ref. 34
Ni XXVII <i>w</i>	1.5886	1.5856	1.5885	1.5879	1.588 48	1.588 26
Ni XXVI <i>x</i>	1.5925	1.5897	1.5926	1.5918	1.592 36	1.592 20
<i>t</i>	1.5940	1.5911	1.5940	1.5934		
<i>y</i>	1.5966			1.5959	1.596 56	1.596 32
<i>q</i>	1.5972	1.5941	1.5970	1.5965		
<i>k</i>	1.5987	1.5956	1.5985	1.5980		
<i>r</i>	1.5999	1.5973	1.6002	1.5992		
<i>j</i>	1.6011	1.5983	1.6012	1.6005		
<i>z</i>	1.6038	1.6010	1.6039	1.6031	1.603 64	1.603 39
Ni XXV β	1.6046	1.6015	1.6044			
$1s2s2p^2\ ^3D_3 - 1s^22s2p\ ^3P_2$	1.6090	1.6064	1.6093			
$1s2s2p^2\ ^1D_2 - 1s^22s2p\ ^1P_1$	1.6110	1.6087	1.6116			
Ni XXIV $1s^22s^22p\ ^2S_{1/2} - 1s^22s^22p\ ^2P_{3/2}$	1.6123	1.6097	1.6126			
$1s2s^22p^2\ ^2P_{3/2} - 1s^22s^22p\ ^2P_{3/2}$	1.6135	1.6109	1.6138			
<i>A</i>	1.6144	1.6117	1.6146			
<i>B</i>	1.6144	1.6118	1.6147			
<i>C</i>	1.6167	1.6141	1.6170			

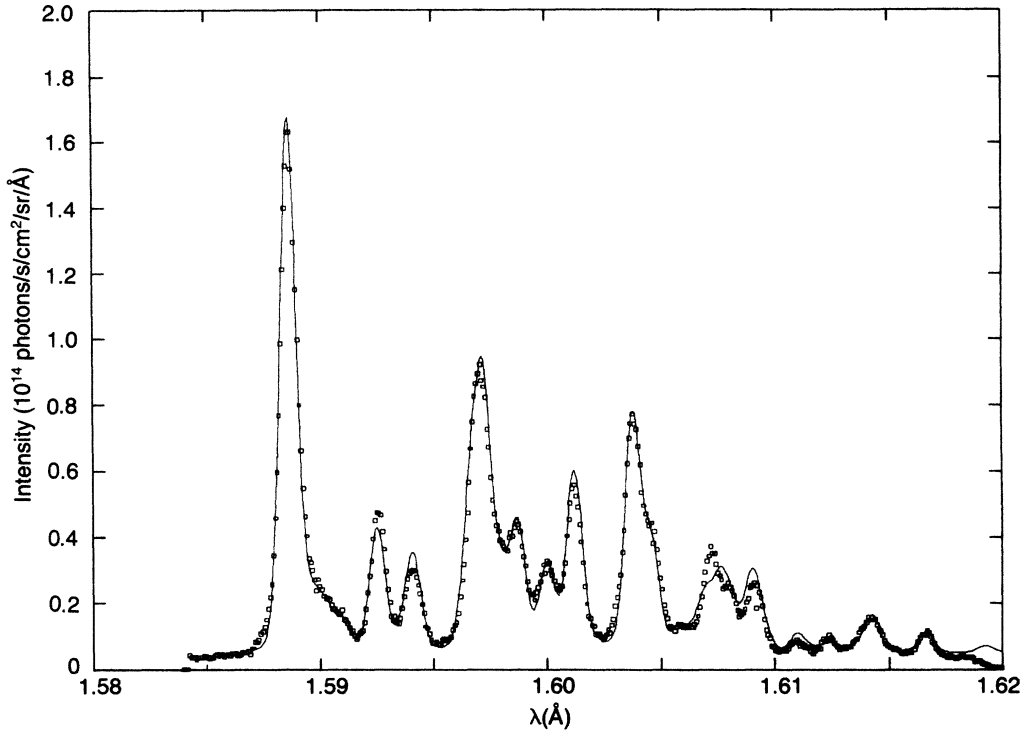


FIG. 6. Simulated spectral intensities of heliumlike nickel and satellites for a peak on-axis electron temperature $T_e = 2.8$ keV, but with the ionization equilibrium populations increased by factors of 1.75, 1.5, and 2.5 for the lithium, beryllium, and boronlike ionization stages, respectively, from the values calculated using the data of Ref. 29. The spectral line wavelengths are deduced from the experimental spectrum (see Table X). Voigt line profiles with a Gaussian width corresponding to an ion temperature of 2.39 keV and a Lorentzian width corresponding to one channel have been used.

ratio of 1.8. This shows that there is a contribution from inner-shell excitation of the B-like ion to the feature ($A + B$), while such a contribution is not possible for the line C as this line is not accessible by direct excitation from the ground level and two-stage excitation via the $1s^2 2s^2 2p^2 P_{3/2}$ level (see Table VIII) is negligible for $N_e < 10^{15} \text{ cm}^{-3}$. The observations imply a proportion of 55% of the feature at ($A + B$) as being due to inner-shell excitation.

The relative abundance ratios deduced from the best fit to the experimental data including integration along the spectrometer line of sight are 0.7, 0.2, and 0.06 for Ni XXVI/Ni XXVII, Ni XXV/Ni XXVII, and Ni XXIV/Ni XXVII, respectively. Theoretical values for a coronal equilibrium distribution deduced from the data of Ref. 29 for a central electron temperature of 2.8 keV are 0.330, 0.090, and 0.017, respectively (a peak electron temperature of 3.1 keV gives the corresponding values of 0.275, 0.061, and 0.0097). This comparison clearly shows discrepancies between the population ratios of the lithiumlike to boronlike ions relative to the heliumlike ions and the theoretical values. Effects which could cause such discrepancies between the experimentally determined lithiumlike to boronlike population and theory are discussed briefly below.

(i) Inaccurate electron temperature. The observed intensities of berylliumlike and boronlike lines seem to imply in the plasma center electron temperatures of 2.3 keV assuming coronal equilibrium calculated with the

data of (Ref. 29) or lower (assuming the coronal ionization balance data of Refs. 35–37), which are well outside the error range possible for any of the electron-temperature diagnostics of JET (see Refs. 30 and 38).

(ii) Uncertainties in the ionization-recombination rate coefficients of the lithiumlike to boronlike ions. There are two possibilities here.

(a) Uncertainties in the ionization-recombination rate coefficients. Errors of up to a factor 2 are usually assumed to be possible in calculated ionization balances between ionization stages. Estimates of the experimental ratio of the Ni XXIV/Ni XXVII populations vary from calculations using the data of Ref. 29 by a factor ~ 3 and by larger factors if we compare to the tabulations of Refs. 35–37).

(b) Uncertainties in the excitation rates, autoionization, and radiative probabilities. The ability to obtain a good agreement between the observed and simulated spectra (see Fig. 6) implies that these atomic data are accurate to within 10%. If the atomic rates were not very accurate, the adjustment would require as many parameters as there are lines. Only three parameters are adjusted for approximately 15 significant lines.

(iii) Hollow impurity profiles. Instead of the ratio of the nickel density to electron density being constant over the plasma profile as assumed for the simulations of this paper, the ratio could change with minor radius. Measurements of nickel concentration in JET from observations of emission from lower ionization stages, i.e., emis-

sion from the plasma edge (e.g., Ni XVII),⁹ agree to within the estimated accuracies of the measurements (approximately a factor 2–3) with nickel concentrations deduced using our heliumlike nickel resonance line intensities which are emitted in the plasma center. Simulations (as for Fig. 5) with a factor 2 increase of nickel concentration from the center to the edge of the plasma only produce a small variation of the relative satellite intensities.

(iv) Charge-exchange recombination with thermal background hydrogen. Estimates indicate that charge-exchange recombination does not alter the populations of hydrogenlike to boronlike nickel ions at the neutral density values measured in the center of JET by neutral-particle analyzers, but may do so at positions at and beyond the half minor radius (see the Appendix). Charge exchange could also cause extra emission here by directly populating higher quantum states of the ions without necessarily changing the ionization balance.

(v) Transport. The effect of the inward transport of Ni impurity ionization stages from the tokamak edge to the center for hydrogenlike to boronlike satellite emission varies from negligible (hydrogenlike to berylliumlike) to small (boronlike) for the impurity diffusion coefficient $D \simeq 10\,000\text{ cm}^2/\text{sec}$ and inward drift velocities $v \simeq 400\text{ cm/s}$ measured in JET.⁹ These values of D and v have been determined using vuv spectroscopy of the decay of accidental metal injections and by observing in the vuv the position and width of impurity emission shells. With different D and v values and possibly radial dependencies in these parameters the effect of transport might become noticeable.

It seems that effects (i), (ii), and (iii) are probably not significant [although uncertainties mentioned in (iia) are significant in this comparison] but that processes (iv) and (v) may have effects on the emission of at least some of the lithiumlike to boronlike satellites. One of them, or possibly both acting together, could produce the discrepancies. In the absence of more quantitative information, we can heuristically adjust the lithiumlike to boronlike ion populations in our simulations of the spectra to obtain agreement of simulated spectra with the experimental spectrum.

The population of the lithiumlike to boronlike ions across the profile are adjusted by a constant factor for each ionization stage in Fig. 6. In order to obtain agreement of the simulation with the experimental spectrum, we need populations which are 1.75 times the lithiumlike populations, 1.5 times the berylliumlike populations, and 2.5 times the boronlike populations obtained from Ref. 29 if the central, on-axis electron temperature is taken to be 2.8 keV. Since the full spectrum is composed of spectra from different plasma shots there might be small variations from shot to shot in plasma parameters, i.e., also in the ion stage abundances. In particular there is an underestimate of the emission at 1.607 Å. However, a simulation of the spectrum in the region 1.603–1610 Å with a larger Li-like abundance cannot give a better fit than the one presented in Fig. 6.

In the Fig. 6 plot, the calculated spectra are convoluted with a Lorentzian line profile which has a half width

equal to the natural broadening of the He-like Ni resonance line. This results in better fits to the experimental spectra compared to Fig. 5 where simple Gaussian profiles are assumed. The Fig. 6 fits are also improved by using the spectral line wavelengths deduced from the experimental spectrum (see Table X).

B. Hydrogenlike spectrum

The experimentally determined wavelengths of the hydrogenlike Lyman- α_1 and - α_2 lines are listed and compared with calculations from various authors^{26,32,39} in Table XI. The wavelength separation of the doublet components is also shown.

The intensity ratio of the Lyman- α doublet components observed experimentally [Fig. 2(b)] is approximately 0.6, which is the ratio to be expected from theory (Sec. III B) after taking into account the contribution to the Lyman- α_2 intensity from the magnetic dipole ($2s\ ^2S_{1/2} - 1s\ ^2S_{1/2}$) line. The theoretical spectrum from the data of Table IX is fitted to the experimental spectrum [Fig. 2(b)] in Fig. 7. The spectrum is made up of 74 lines. Again, unknown parameters in the calculated spectrum which are adjusted to optimize the fit are the level of continuum, background emission, the fraction of nickel in the plasma, and a wavelength shift of all lines. A wavelength shift was found not to be necessary for the H-like spectrum, but this is probably fortuitous in view of our estimated experimental absolute wavelength measurement error of $\pm 0.001\text{ Å}$. Overall, the calculated and experimental H-like satellite spectrum agree well (see Fig. 7) although the comparison is not as detailed as for the He-like spectra.

VI. CONCLUSIONS

The $n=1$ to $n=2$ spectra have been recorded for heliumlike and hydrogenlike nickel emitted for the JET tokamak with a spectral resolution $\lambda/\Delta\lambda$ of $\sim 20\,000$. Atomic data (wavelengths and intensity factors) have been calculated in a multiconfiguration intermediate coupling scheme using scaled Thomas-Fermi-Dirac potentials and compared with the experimental spectra.

TABLE XI. The wavelengths of the hydrogenlike nickel Lyman- α lines and their separation ($\Delta\lambda$). The relative accuracy of the experimental wavelengths is approximately $\pm 0.0001\text{ Å}$. The absolute accuracy of the experimental wavelengths is approximately 0.001 Å .

	λ_1 (Å)	λ_2 (Å)	$\Delta\lambda$ (mÅ)
	Lyman α_1	Lyman α_2	
Experimental	1.5294	1.5348	5.39
Present calculation	1.5297	1.5350	5.3
Ref. 26	1.5303	1.5358	5.43
Ref. 32	1.5298	1.5351	5.3
Ref. 39	1.5304	1.5358	5.43

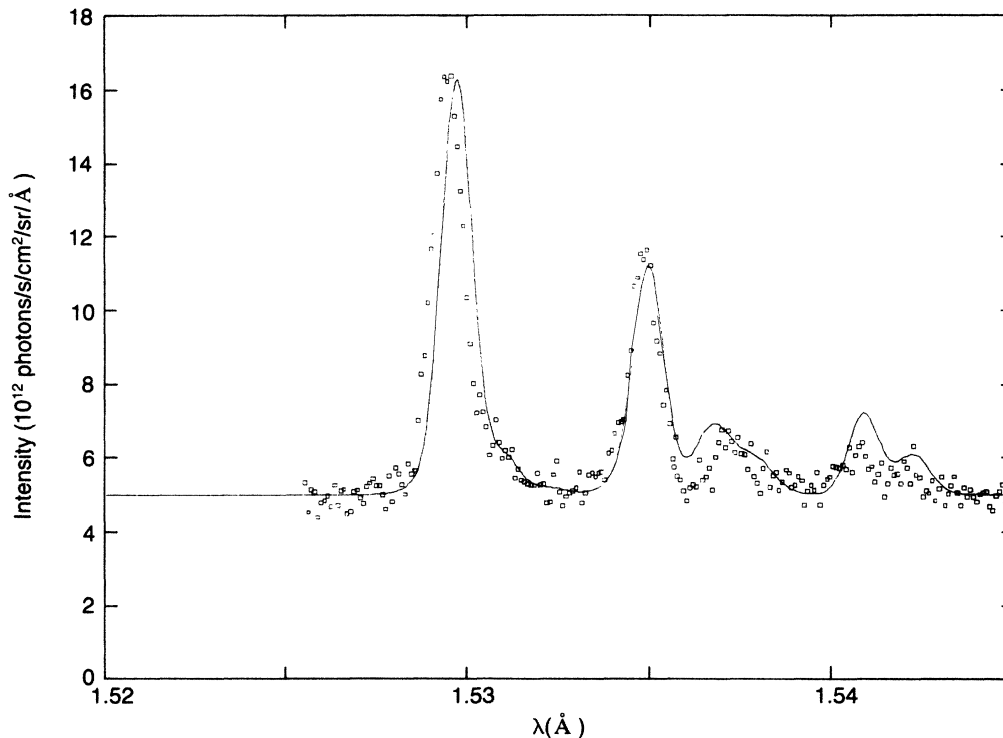


FIG. 7. Calculated spectrum near the hydrogenlike nickel Lyman- α doublet (solid curve) superimposed on the experimental spectrum (data points). Excitation rates of $3.64 \times 10^{-13} \text{ cm}^3 \text{ sec}^{-1}$ and $1.82 \times 10^{-13} \text{ cm}^3 \text{ sec}^{-1}$ have been used for α_1 and α_2 , respectively (Ref. 27). The two joining spectra have been normalized to the same background (normalization factor of 0.870).

Overall good agreement between theory and the experimental spectra is obtained though the intensities of satellite lines relative to resonance lines from the heliumlike to boronlike ions indicate population ratios of lithiumlike to boronlike ions relative to the heliumlike ions greater than expected for a coronal ionization balance.

ACKNOWLEDGMENTS

We would like to acknowledge the JET team for producing the plasmas, technical support, help in analysis, and providing other diagnostic information. In particular, it is a pleasure to acknowledge K. Behringer, G. Bracco, W. Engelhardt, N. Foden, G. Magyar, B. Oliver, H. Summers, M. Shaw, and B. Viacoz. In the construction of the spectrometer, the authors are indebted to several colleagues from the ENEA Laboratory, Frascati, in particular, R. Bartiromo for his leading role in the design and construction and L. Panaccione, S. Mantovani, and G. Pizzicaroli for their collaboration in all the phases of the spectrometer realization. The atomic physics computations have been carried out on the NAS 9080 computer of the Centre International de Calcul Electronique (CIRCE) Orsay, France.

APPENDIX

In this appendix we show that charge-exchange recombination of highly stripped nickel ions with thermal background hydrogen should not significantly alter the populations of hydrogenlike to boronlike nickel

in the center of the JET tokamak, but may do so at positions at and beyond the half minor radius. To do this, we will compare the rates of recombination due to radiative and dielectronic processes with estimates of the rates of charge-exchange recombination. The rate R_c of radiative and dielectronic recombination of an ion Ni^{z+} of population density N_z to $\text{Ni}^{(z-1)+}$ is given by

$$R_c = \alpha_c N_e N_z, \quad (\text{A1})$$

where α_c is the rate coefficient for recombination and N_e is the electron density, while the rate of charge-exchange recombination from Ni^{z+} to $\text{Ni}^{(z-1)+}$ is given by

$$R_e = N_H N_z \langle \sigma v \rangle, \quad (\text{A2})$$

where σ is the cross section for a charge-exchange collision, v is the relative velocity of the neutral hydrogen atoms and the nickel ions, and N_H is the density of neutral hydrogen.

For charge exchange to be negligible compared to radiative and dielectronic recombination, we require

$$R_c \gg R_e,$$

which implies that

$$\frac{N_H}{N_e} \ll \frac{\alpha_c}{\langle \sigma v \rangle}. \quad (\text{A3})$$

We may estimate that $\alpha_c \geq 10^{-12} \text{ cm}^3 \text{ sec}^{-1}$ (Ref. 28), $\sigma \sim 10^{-14} \text{ cm}^2$ (Refs. 40–42) and that $v \lesssim 10^8 \text{ cm sec}^{-1}$, giving from Eq. (A3)

$$\frac{N_H}{N_e} \ll 10^{-6} \quad (\text{A4})$$

as the condition for charge exchange to have a negligible effect on the Ni^{z+} population.

For the series of JET pulses used to obtain the spectra for Fig. 2(a), neutral-particle analyzers⁴³ have measured

thermal, background hydrogen neutral densities at the plasma center such that $N_H/N_e \approx 5 \times 10^{-8}$ increasing to $N_H/N_e \approx 10^{-6}$ at around half of the minor radius. Charge exchange is, therefore, not a significant effect on the population of the highly ionized nickel ions at the plasma center, but may be important at positions around and beyond half the minor radius.

*Permanent address: Associazione EURATOM-Comitato Nazionale per la Ricerca e per lo Sviluppo dell'Energia Nucleare e delle Energie Alternative (ENEA) sulla Fusione, Centro Ricerche Energia Frascati, Casella Postale 65, I-00044 Frascati, Roma, Italy.

[†]Permanent address: Laser Division, Rutherford Appleton Laboratory, Chilton, Didcot, Oxfordshire OX11 0QX, England.

¹E. Källne and J. Källne, *Phys. Scr. T* **7**, 152 (1987).

²S. Morita and J. Fujita, *Nucl. Instrum. Methods Phys. Res. B* **9**, 713 (1985); B. S. Fraenkel and J. L. Schwob, *Phys. Lett.* **40A**, 83 (1972); Y. V. Sidelnikov, E. Y. Kononov, and K. N. Koshelev, *Nucl. Instrum. Methods Phys. Res. B* **9**, 724 (1985).

³H. Hsuan, M. Bitter, K. W. Hill, S. von Goeler, B. Grek, D. Johnson, L. C. Johnson, S. Sesnic, C. P. Bhalla, K. R. Karim, F. Bely-Dubau, and P. Faucher, *Phys. Rev. A* **35**, 4280 (1987).

⁴P. H. Rebut, R. J. Bickerton, and B. E. Keen, *Nucl. Fus.* **25**, 1011 (1985).

⁵J. Jacquinet, V. Bhatnagar, H. Brinkschulte, M. Bures, S. Corti, G. A. Cottrell, M. Evrard, D. Gambier, A. Kaye, P. P. Lallia, F. Sand, C. Schueller, A. Tanga, K. Thomsen, and T. Wade, *Philos. Trans. R. Soc. London, Ser. A* **322**, 95 (1987).

⁶G. Duesing, P. Lomas, A. Stabler, P. Thomas, and E. Thompson, *Philos. Trans. R. Soc. London, Ser. A* **322**, 109 (1987).

⁷P. H. Rebut *et al.*, JET Report No. IAEA-CN-47/A-I-2 (unpublished).

⁸J. P. Coad, K. H. Behringer, and K. J. Dietz, *J. Nucl. Mater.* **145-147**, 747 (1987).

⁹K. H. Behringer *et al.*, *Nucl. Fus.* **26**, 751 (1986).

¹⁰R. Giannella, F. Bombarda, E. Källne, L. Panaccione, and G. Tallents, *Bull. Am. Phys. Soc.* **31**, 1590 (1986).

¹¹R. Bartiromo, F. Bombarda, R. Giannella, S. Mantovani, F. Panaccione, and G. Pizzicaroli (unpublished).

¹²H. H. Johann, *Z. Phys.* **69**, 185 (1931).

¹³R. Bartiromo, R. Giannella, M. L. Apicella, F. Bombarda, S. Mantovani, and G. Pizzicaroli, *Nucl. Instrum. Methods* **225**, 378 (1984).

¹⁴F. Bely-Dubau, J. Dubau, P. Faucher, A. H. Gabriel, M. Loulergue, L. Steenman Clark, S. Volonté, E. Antonucci, and C. Rapley, *Mon. Not. R. Astron. Soc.* **201**, 115 (1982).

¹⁵TFR Group, J. Dubau, and M. Loulergue, *J. Phys. B* **15**, 1007 (1981).

¹⁶W. Eissner, M. Jones, and H. Nussbaumer, *Comput. Phys. Commun.* **8**, 270 (1974).

¹⁷W. Eissner and M. J. Seaton, *J. Phys. B* **5**, 2187 (1972).

¹⁸H. E. Saraph, *Comput. Phys. Commun.* **3**, 246 (1972).

¹⁹TFR Group, F. Bombarda, F. Bely-Dubau, P. Faucher, M. Cornille, J. Dubau, and M. Loulergue, *Phys. Rev. A* **32**,

2374 (1985).

²⁰A. H. Gabriel, *Mon. Not. R. Astron. Soc.* **160**, 99 (1972).

²¹P. Faucher and J. Dubau, *Phys. Rev. A* **31**, 3672 (1985).

²²F. Bely-Dubau, J. Dubau, P. Faucher, and A. H. Gabriel, *Mon. Not. R. Astron. Soc.* **198**, 239 (1982).

²³M. Bitter, K. W. Hill, N. R. Sauthoff, P. C. Efthimion, E. Meservey, W. Roney, S. von Goeler, R. Horton, M. Goldman, and W. Stodieck, *Phys. Rev. Lett.* **43**, 129 (1979).

²⁴M. Bitter, K. W. Hill, M. Zarnstoff, S. von Goeler, R. Hulse, L. C. Johnson, N. R. Sauthoff, S. Sesnic, K. M. Young, M. Tavernier, F. Bely-Dubau, P. Faucher, M. Cornille, and J. Dubau, *Phys. Rev. A* **32**, 3011 (1985).

²⁵H. E. Mason and P. J. Storey, *Mon. Not. R. Astron. Soc.* **191**, 631 (1980).

²⁶P. J. Mohr, *At. Data Nucl. Data Tables* **29**, 453 (1983).

²⁷L. Blanchet, M. Cornille, J. Dubau, P. Faucher, J. Lion, and S. Volonté, *Astron. Astrophys.* **152**, 417 (1985).

²⁸G. J. Tallents, *J. Phys. B* **18**, 3299 (1985).

²⁹Ionization rates from A. Burgess and M. C. Chidichimo, *Mon. Not. R. Astron. Soc.* **203**, 1269 (1983); radiative recombination rates from S. von Goeler *et al.*, *Nucl. Fus.* **15**, 301 (1975); and dielectronic recombination rates from D. E. Post *et al.*, *At. Data Nucl. Data Tables* **20**, 397 (1977). Tabulated by A. E. P. M. Abel-van Mannen, JET Report No. JET-DN-T(85)29 (unpublished).

³⁰D. V. Bartlett, E. A. M. Baker, D. J. Campbell, and A. E. Costley, *Rev. Sci. Instrum.* **56**, 940 (1985).

³¹D. Veron, Report No. Eur8351-II-EN, p. 283.

³²L. A. Vainshtein and U. I. Safronova, *Atom. Data Nucl. Data Tables* **21**, 49 (1978).

³³L. A. Vainshtein and U. I. Safronova, *Phys. Scr.* **31**, 519 (1985).

³⁴C. Corliss and J. Sugar, *J. Phys. Chem. Ref. Data* **10**, 197 (1981).

³⁵V. L. Jacobs, J. Davis, J. E. Rogerson, M. Blaha, J. Cain, and M. Davis, *Astrophys. J.* **239**, 1119 (1980).

³⁶M. Arnaud and R. Rothenflug, *Astron. Astrophys. Suppl. Ser.* **60**, 425 (1985).

³⁷J. M. Shull and M. Van Steenberg, *Astrophys. J. Suppl. Ser.* **48**, 95 (1982).

³⁸D. Pasini *et al.* (unpublished).

³⁹G. W. Erickson, *J. Phys. Chem. Ref. Data* **6**, 831 (1977).

⁴⁰H. Ryufuku and T. Watanabe, *Phys. Rev. A* **20**, 1528 (1979).

⁴¹R. K. Janev and P. Hvelplund, *Comments At. Mol. Phys.* **11**, 75 (1981).

⁴²G. J. Tallents and B. Luther-Davies, *J. Phys. D* **15**, L125 (1982).

⁴³S. Corti *et al.* (unpublished).

⁴⁴M. H. Chen, B. Crasemann, and H. Mark, *Phys. Rev. A* **24**, 1852 (1981).